Surv Geophys (2008) 29:139–186
DOI 10.1007/s10712-008-9045-z

ORIGINAL PAPER

3-D Global Induction in the Oceans and Solid Earth: Recent Progress in Modeling Magnetic and Electric Fields from Sources of Magnetospheric, Ionospheric and Oceanic Origin

A. V. Kuvshinov

Received: 1 April 2008 / Accepted: 18 July 2008 / Published online: 10 October 2008

Abstract Electromagnetic induction in the Earth's interior is an important contributor to the near-Earth magnetic and electric fields. The oceans play a special role in this induction due to their relatively high conductivity which leads to large lateral variability in surface conductance. Electric currents that generate secondary fields are induced in the oceans by two different processes: (a) by time varying external magnetic fields, and (b) by the motion of the conducting ocean water through the Earth's main magnetic field. Significant progress in accurate and detailed predictions of the electric and magnetic fields induced by these sources has been achieved during the last few years, via realistic three-dimensional (3-D) conductivity models of the oceans, crust and mantle along with realistic source models. In this review a summary is given of the results of recent 3-D modeling studies in which estimates are obtained for the magnetic and electric signals at both the ground and satellite altitudes induced by a variety of natural current sources. 3-D induction effects due to magnetospheric currents (magnetic storms), ionospheric currents (Sq, polar and equatorial electrojets), ocean tides, global ocean circulation and tsunami are considered. These modeling studies demonstrate that the 3-D induction (ocean) effect and motionally-induced signals from the oceans contribute significantly (in the range from a few to tens nanotesla) to the near-Earth magnetic field. A 3-D numerical solution based on an integral equation approach is shown to predict these induction effects with the accuracy and spatial detail required to explain observations both on the ground and at satellite altitudes.

Keywords Global EM induction · 3-D numerical modeling · Ocean effect · Magnetospheric and ionospheric sources · Ocean tides · Global ocean circulation · Tsunami

On leave from Institute of Terrestrial Magnetism, Ionosphere and Radiowave Propagation, Russian Academy of Sciences, 142190 Troitsk, Moscow region, Russia.

A. V. Kuvshinov (✉)
Institute of Geophysics, ETH, 8093 Zurich, Switzerland
e-mail: kuvshinov@erdw.ethz.ch

1 Introduction

Global electromagnetic (EM) induction studies have been the focus of increasing attention during the past few years. A primary stimulus for this interest has been the tremendous recent growth in the amount of global geomagnetic data available, especially from recent low-Earth-orbiting (LEO) satellite missions (see Table 1). These satellites measure (or measured) the magnetic fields from their circular polar orbits with unprecedented accuracy (cf. Neubert et al. 2001; Reigber et al. 2002). Moreover the geomagnetic LEO three-satellite constellation mission *Swarm* involving two satellites flying at 450 km, and a third at 550 km is scheduled to be launched by the European Space Agency in 2010 (cf. Friis-Christensen et al. 2006). In contrast to land-based data from geomagnetic observatories, which are sparsely and irregularly distributed with only a few being found in oceanic regions, satellite-borne measurements provide an excellent spatio-temporal coverage with high-precision data of uniform quality. In addition to satellite and observatory measurements, variations of voltage differences measured in transoceanic submarine telecommunication cables have been recently used for deep EM studies in oceanic regions (e.g. Lanzerotti et al. 1992; Vanyan et al. 1995; Fujii and Utada 2000; Utada et al. 2003; Kuvshinov et al. 2005).

The combination of land- and ocean-based observations with satellite-borne measurements presents an excellent opportunity to attack the most challenging problem of deep EM studies: the recovery of three-dimensional (3-D) variations of electrical conductivity in the Earth's mantle, beneath the oceans as well the continents. Since conductivity reflects the connectivity of constituents such as graphite, fluids, partial melt, and volatiles (all of which may have profound effect on rheology), 3-D conductivity images could provide very valuable information about mantle convection and the processes underlying tectonic activity in the Earth. However, the efficiency of the 3-D inversion of global induction data depends critically on the ability to carry out fast and robust predictions of magnetic/electric signals and responses—this topic provides the focal point of the present review.

A second reason for recent interest in global EM induction studies is that investigations of the core field and the geodynamo, as well as the mapping of lithospheric magnetization and its geologic interpretation, require the construction of field models that are contaminated as little as possible by fields originating from the ionosphere and magnetosphere and from their Earth-induced counterparts. Accurate extraction of the latter contributions from the magnetic signals measured by satellites is a nontrivial problem. So far even the most sophisticated modeling schemes (e.g., the Comprehensive Model CM4 of Sabaka et al. 2004) have assumed the conducting Earth to be spherically symmetric (1-D). As a consequence, the EM effects and/or signals originating in the oceans have been ignored. In this review, it will be demonstrated that the oceans play a special role in the EM induction problem due to their relatively high conductance and due to the large departures from spherical symmetry in their conductance.

Table 1 Modern LEO satellites carrying out magnetic measurements

Name	Launch	Lifetime	Altitude (km)	Local time (LT)	Data type
Oersted	February 1999	Still in operation	630–880	All LT	Vector (until 2007), Scalar
CHAMP	July 2000	Still in operation	350–450	All LT	Vector, Scalar
SAC-C	November 2000	2005	700	10:30/22:30	Scalar

Recent interest in global EM induction has also resulted from the significant methodological progress made during the last few years that has enabled accurate and detailed numerical calculations of induced magnetic and electric fields in 3-D spherical geometry. It is now possible to tackle various global induction problems involving high levels of complexity and spatial detail in both the electrical conductivity models and the sources.

In this paper, a review is presented of recent results of 3-D numerical modeling that quantitatively estimates magnetic and electric signals at both the ground and satellite altitudes induced by a variety of realistic sources. The structure of the paper is as follows. Section 2 describes the 3-D conductivity model of the Earth relevant for global induction. Section 3 briefly outlines the equations governing global induction and their solution. Sections 4–9 describe 3-D induction resulting from magnetospheric storms, ionospheric currents (Sq and EEJ, convection polar electrojets in North and South polar regions), ocean tides, ocean circulation and a tsunami, respectively. The conclusions are presented in Sect. 10. The paper also includes two Appendices that summarize the integral equation approach used to produce many of the results presented.

2 3-D Conductivity Model

Electromagnetic (EM) induction simulations require a model of the electrical conductivity of the Earth. Our basic 3-D model consists of a thin spherical layer of variable conductance $S(\vartheta,\varphi)$ at the Earth's surface and a radially symmetric spherical conductivity $\sigma(r)$ underneath. The shell conductance $S(\vartheta,\varphi)$ is obtained by considering contributions both from sea-water and from sediments. The conductance of the sea water has been taken from Manoj et al. (2006a) and accounts for ocean bathymetry (taken from the global $5' \times 5'$ NOAA ETOPO map of bathymetry/topography), ocean salinity, temperature and pressure as given by the World Ocean Atlas 2001 (www.ngdc.noaa.gov). Conductance of the sediments (in continental as well as oceanic regions) is based on the global sediment thicknesses given by the $1^\circ \times 1^\circ$ map of Laske and Masters (1997) and calculated by a heuristic procedure similar to that described in Everett et al. (2003). The upper plot of Fig. 1 presents the map of the adopted surface shell conductance (at $1^\circ \times 1^\circ$ resolution in co-latitude and longitude). Note that this grid size is generally used in the following sections to solve the induction equations and to calculate the magnetic and electric fields. The lower plot of Fig. 1 shows the same map of conductance but uses a logarithmic scale: it illustrates that not only the oceans but also the continents possess variable conductance; we shall see later that these inland inhomogeneities are of relevance at short periods. Note that the surface thin layer model is applicable for periods from a few hours and longer, where the layer thickness is much smaller than the penetration depth of the EM field. This, in particular, means that for calculations at shorter periods (10 min and less), the surface thin layer model is replaced by a model which explicitly accounts for the variability of the surface layer thickness, which is primarily derived from the ocean bathymetry. Thus, during calculations of induction at short periods, the surface layer has been subdivided into 3 non-uniform layers each of 4 km thickness. In addition a more dense mesh (of $0.3^\circ \times 0.3^\circ$ resolution) in the lateral direction was used for these calculations.

The underlying spherically symmetric (1-D) conductivity model consists of a 100 km resistive lithosphere of 3000 Ω m and a layered model underneath, derived from 5 years of CHAMP, Ørsted, and SAC-C magnetic data by Kuvshinov and Olsen (2006); this model is shown in Fig. 2.

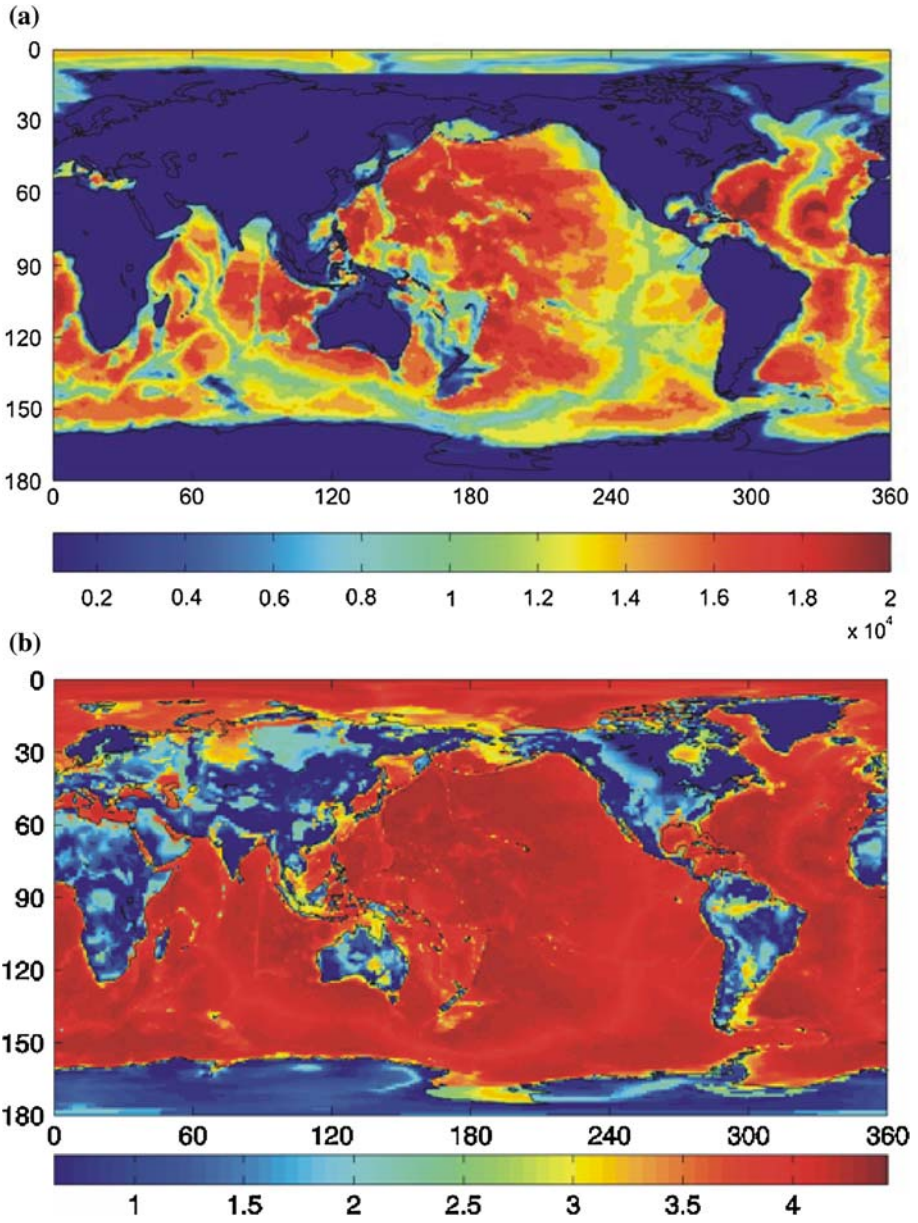

Fig. 1 (**a**) Map of the adopted surface shell conductance (S), based on ocean bathymetry, salinity, temperature and pressure, as well as on sedimentary thickness (after Manoj et al. (2006a). (**b**) Map of the adopted surface shell conductance map, on a logarithmic scale (log S)

3 Prediction of Magnetic and Electric Fields

The results presented in this review rely on the solution of the 3-D forward problem. This involves prediction of the EM fields induced by a given time-varying source in the specified spherical 3-D conductivity model of the Earth. Assuming that the considered

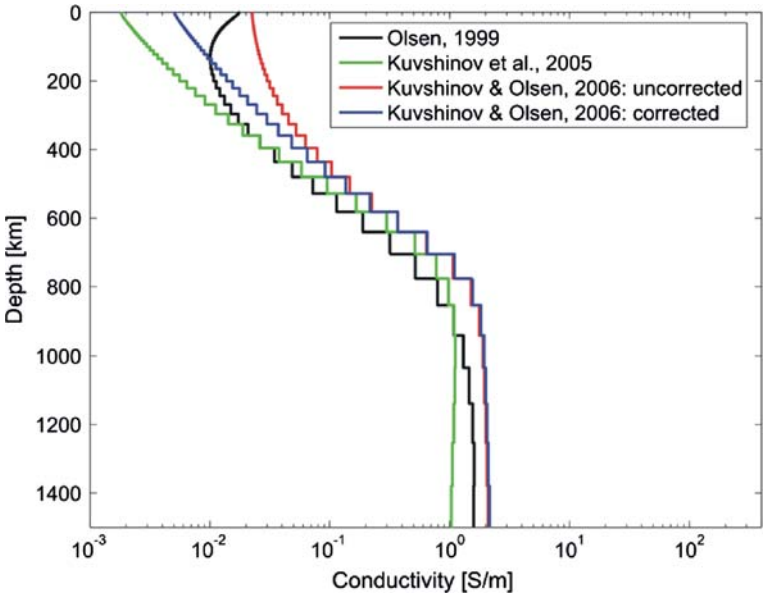

Fig. 2 Adopted 1-D conductivity (blue curve) beneath the surface shell along with other 1-D conductivity profiles. See Kuvshinov and Olsen (2006) for further details

sources can be converted into the frequency domain by Fourier transformation, the electric and magnetic fields, **E** and **H**, obey Maxwell's equations

$$\nabla \times \mathbf{H} = \sigma \mathbf{E} + \mathbf{j}^{ext}, \quad \nabla \times \mathbf{E} = i\omega\mu_0 \mathbf{H} \tag{1}$$

where $\mathbf{j}^{ext}$ is the impressed (extraneous) current (given source), $i = \sqrt{-1}$, σ is the given conductivity distribution in the model, and the time factor is $\mathrm{e}^{-i\omega t}$. The magnetic permeability is assumed to be that of free space, μ_0, everywhere.

Above the conducting Earth ($r > a$, $a = 6371.2$ km is the mean Earth's radius) and beneath the external (magnetospheric and ionospheric) sources, the Fourier component of the magnetic field, $\mathbf{B}(\omega) = \mu_0 \mathbf{H} = -\mathrm{grad}\, V(\omega)$, can be derived from a scalar magnetic potential, V, which is represented by a spherical harmonic expansion

$$V(r, \vartheta, \varphi, \omega) = a \sum_{n=1}^{\infty} \sum_{m=-n}^{m} \left[\varepsilon_n^m(\omega) \left(\frac{r}{a}\right)^n + \imath_n^m(\omega) \left(\frac{a}{r}\right)^{n+1} \right] P_n^m(\cos\vartheta)\, \mathrm{e}^{im\varphi}, \tag{2}$$

where r, ϑ and φ are the distance from the Earth's center, co-latitude and longitude respectively, ε_n^m and $\imath_n^m$ are the complex expansion coefficients of the external (inducing) and internal (induced) parts of the potential, and $P_n^m(\cos\vartheta)$ are associated Legendre polynomials. Components of the magnetic field follow from this potential expansion as

$$B_r(r, \vartheta, \varphi, \omega) = -\sum_{n=1}^{\infty} \sum_{m=-n}^{m} \left[n\varepsilon_n^m(\omega) \left(\frac{r}{a}\right)^{n-1} - (n+1)\imath_n^m(\omega) \left(\frac{a}{r}\right)^{n+2} \right] P_n^m(\cos\vartheta)\, \mathrm{e}^{im\varphi}, \tag{3}$$

$$B_\vartheta(r, \vartheta, \varphi, \omega) = -\sum_{n=1}^{\infty} \sum_{m=-n}^{m} \left[\varepsilon_n^m(\omega) \left(\frac{r}{a}\right)^{n-1} + \imath_n^m(\omega) \left(\frac{a}{r}\right)^{n+2} \right] \frac{dP_n^m(\cos\vartheta)}{d\vartheta} \mathrm{e}^{im\varphi}, \tag{4}$$

$$B_\varphi(r,\vartheta,\varphi,\omega) = -\sum_{n=1}^{\infty}\sum_{m=-n}^{m}\left[\varepsilon_n^m(\omega)\left(\frac{r}{a}\right)^{n-1} + \iota_n^m(\omega)\left(\frac{a}{r}\right)^{n+2}\right]\frac{im}{\sin\vartheta}P_n^m(\cos\vartheta)\,\mathrm{e}^{im\varphi}. \quad (5)$$

From Eqs. 3–5 it is seen, in particular, that the radial component is to a greater extent (than the horizontal components) influenced by induction. Indeed, for the horizontal components the degree of this influence is governed by the (complex) Q-response, which is the ratio of the internal to external coefficients for a specific degree, order and frequency. In the case of a 1-D conductivity distribution ($\sigma \equiv \sigma(r)$), each external coefficient induces only one internal coefficient (of the same degree n and order m); their ratio Q is independent of m

$$Q_n(\omega) = \iota_n^m(\omega)/\varepsilon_n^m(\omega), \quad (6)$$

and can be calculated using appropriate recurrence formulas (see, for example, Eqs. A.2.30 and A.2.35 of Appendix 2). For the radial component, the degree of the influence is governed by the quantity

$$Q_n^{(r)} \equiv \frac{n+1}{n}Q_n(\omega). \quad (7)$$

This means that the relative amount of induction (compared with the external part) in the radial component is $\frac{n+1}{n}$ times larger for individual terms than for the horizontal components. In addition, due to subtraction in the radial component, the ratio of induced signal to total (external + induced) signal is much bigger.

Figure 3 presents $|Q_n^{(r)}|$ for a range of periods of inducing field with respect to degree n. Colored dashed and solid lines depict the results for the 1-D conductivity mantle with and without oceans, respectively. Solid black lines below the plot show the range of degree n of the different sources. For comparison, the dotted line in both plots shows an upper limit, 1, for $|Q_n^{(r)}|$ which corresponds to a perfectly conducting Earth. In this case, induction cancels the radial component at the surface of the Earth and doubles (more or less) the horizontal component. For a period of 2 min, the responses are close (at least up to degree $n = 10$) to the responses for a perfectly conducting Earth. For all n, the longer the period the smaller is $|Q_n^{(r)}|$. $|Q_n^{(r)}|$ also decreases with increasing n. For example, at a period of 24 h, $|Q_n^{(r)}|$ drops from 0.56 for $n = 2$ (degree of fundamental spherical harmonic of Sq at this period) to less than 0.03 for $n = 20$. Inclusion in the 1-D conductivity model of the uniform ocean of 15,000 S conductance substantially changes the $|Q_n^{(r)}|$ behavior. $|Q_n^{(r)}|$ values are then larger in the model with oceans (more induction): for example, at a period of 24 h, and for $n = 2$, $|Q_n^{(r)}|$ increases to 0.81. With the same tendency of decrease with increasing n, $|Q_n^{(r)}|$ remains substantial (0.21) for $n = 20$ at a period of 24 h.

So far the case when the conductivity varies only with depth has been discussed. In the general case of a 3-D electrical conductivity distribution in the Earth ($\sigma \equiv \sigma(r,\vartheta,\varphi)$), each external coefficient ε_n^m induces a whole spectrum of internal coefficients, and thus calculation of the internal (induced) part of magnetic and electric fields requires the numerical solution of Maxwell's equations (1).

During the last two decades a number of algorithms have been developed to solve Maxwell's equations for spherical 3-D conductivity models suitable for applications to the Earth. For frequency-domain forward calculations we have now a number of 3-D solvers based on finite-difference (Uyeshima and Schultz 2000), finite-element (Everett and Schultz 1996; Weiss and Everett 1998; Yoshimura and Oshiman 2002), volume integral equation (Kuvshinov et al. 2002a; Koyama et al. 2002) and spectral (Tarits 1994; Martinec 1999; Plotkin 2004) methods. Each type of solution has its own advantages and drawbacks.

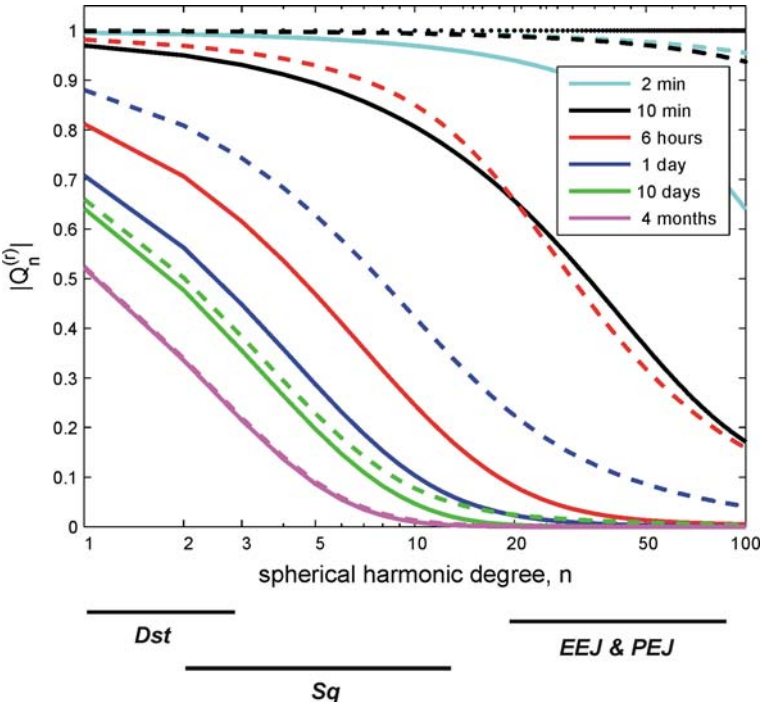

Fig. 3 $|Q_n^{(r)}|$ for different periods as a function of degree n. Solid lines: $|Q_n^{(r)}|$ for the 1-D mantle conductivity model without oceans. Dashed lines: $|Q_n^{(r)}|$ for the 1-D model overlaid by a uniform ocean of 15,000 S. For comparison, the dotted line in the figure shows an upper limit, 1, for $|Q_n^{(r)}|$ which corresponds to a perfectly conducting Earth

The main attraction of the finite-difference (FD) approach is its relatively simple numerical implementation, especially when compared to other approaches, as well as its effectiveness. One then works with a sparse matrix after discretization of the second-order differential equation (either with respect to electric or magnetic fields) deduced from Maxwell's equations (1). The drawback is that the convergence of an iterative solution of the discretized form of the equation is not guaranteed even after pre-conditioning. Note that iterative solution is the only choice for large scale problems. The large computational volume needed for the decay (or stabilization) of EM fields at the boundaries is another disadvantage.

In the finite-element (FE) method, the whole modeling volume is decomposed into elementary volumes (such as prisms, tetrahedrons or volumes of more complex shapes) that specify the geometry of the conductivity model. Accordingly, the electric field (or its potentials) is decomposed via some basic functions and the coefficients of decomposition are sought using the Galerkin method. As with the FD approach, one again arrives at a sparse system of linear equations. The drawbacks of the FD approach generally also apply to the FE approach. The main attraction of the FE solutions is that they are believed to be better able to account for the geometry of the conducting anomalies than other approaches. This attraction is counterbalanced by a nontrivial and usually time-consuming construction of the finite elements themselves.

In spectral methods the quantities of interest are expanded in spherical harmonics in order to represent their lateral variations. Spectral solutions work well with rather smooth

(in the lateral direction) quantities, but cannot adequately describe the field evolution in sub-domains where abrupt changes of conductivity occur (e.g. at the boundary between highly resistive continents and highly conducting oceans).

Finally, with the volume integral equation (IE) method, Maxwell's equations (1) are first reduced to Fredholm's integral equation of the second kind (scattering equation; SE). To derive the SE, a Green's function technique is usually applied. The discretization of the SE yields a linear system resulting in a dense matrix (with all entries filled), but it is much more compact than matrices used in FD and FE methods. The reason for compactness is that in the IE method the modeling region is confined only by the spherical layers that contain the inhomogeneities, whereas in the FD and FE schemes one has to discretize a much larger volume in the radial direction in order to enable the decay (or stabilization) of the fields to be determined. Moreover, the system matrix resulting from modern versions of the IE method does not require preconditioning, whereas the FD and FE methods do, especially for models with large contrasts of conductivity. Nonetheless, many EM software developers refrain from implementing the IE method, because accurate computation of the resulting matrix is a tedious and nontrivial problem.

A small number of time-domain solutions to the 3-D forward induction problem in spherical geometry have been developed. The early solutions were based on a spectral method (Hamano 2002; Velimsky and Martinec 2005) in which the quantities of interest were expanded in spherical harmonics to represent their lateral variations. More recently a method relying on the Fourier transform of frequency-domain IE results Kuvshinov et al. (2006a) has been presented.

The model studies presented in this review rely primarily on the IE method described in the Appendices. The reason for this emphasis is that only IE results (with the exception of results of Tyler et al. (2003), discussed later in the paper) have so far provided published evidence that 3-D global models reproduce the fields in accordance with observations.

4 Magnetospheric Storms

To a first approximation, geomagnetic storms can be described as an intensification of the (westward directed) magnetospheric ring current (e.g. Rostoker et al. 1997). Its time rate of change induces a corresponding internal current system of reversed sign, and hence the major part of the induced currents during storms is eastward directed. While a significant part of the induced currents flow in the open oceans (and in the underlying mantle), coastlines will force them to deviate from the West-East geometry dictated by the external (inducing) currents. This leads to current concentration or/and channeling, which is especially pronounced at the edges of continental barriers like southern Africa.

Numerical modeling studies of the ocean effect using realistic conductivity models have been performed during the past 20 years (Kuvshinov et al. 1990; Takeda 1993; Tarits 1994; Weiss and Everett 1998) to estimate this effect in local C-responses—transfer functions which are used in geomagnetic deep sounding of the Earth. The common understanding was that the ocean effect in the responses becomes negligible for periods greater than a few days. Kuvshinov et al. (2002b) reconsidered the ocean effect by making detailed and systematic model studies in the period range from 1 to 64 days with subsequent comparison of predicted and observed C-responses at a number of coastal observatories. They concluded that, for all considered coastal observatories, sea water is a major contributor to the anomalous behavior of C-responses in the period range up to

20 days. The upper plot of Fig. 4 presents observed and predicted C-responses for the South-African observatory Hermanus. Here the local C-responses are defined as

$$C(\omega) = -\frac{a \tan \vartheta_d}{2} \frac{Z(\omega)}{H(\omega)}, \tag{8}$$

where $a = 6371$ km is the mean radius of the Earth, ϑ^d is the geomagnetic co-latitude, and $Z(\omega)$ and $H(\omega)$ are respectively the vertical and horizontal (directed toward geomagnetic North) components of the geomagnetic field at frequency $\omega = \frac{2\pi}{T}$, where T is the period. The observed responses (black circles with bars) were obtained using the multi-taper spectral estimation technique (cf. Riedel and Sidorenko 1995) as applied to hourly mean time series of the geomagnetic field components recorded at Hermanus observatory in 1957–1958. The observed responses demonstrate an extremely strong anomalous effect: both the real and the imaginary parts of the observed C-responses are larger in magnitude than those of the 1-D simulation (without oceans; blue lines), and the discrepancy increases with decreasing period. In addition, several of the criteria that must be fulfilled for a C-response in order to be compatible with a 1-D conductivity structure (Weidelt 1972), for example, $d\mathrm{Re}C(\omega)/d\omega < 0$, are not fulfilled. This anomalous effect is prominent both in the real and imaginary parts of the response and can be traced for periods up to 20 days, changing the results by 1000 % for a 15 h period, over 200% for a period of 10 days, and 80% at a period of 20 days. Note that the anomalous effect is here defined as the difference between the observed and 1-D model responses, normalized by the 1-D C-response. Red lines show the C-responses calculated for a 3-D model with the oceans using the method described in the Appendices.

The predicted 3-D model C-responses fit the observed responses very well for all periods, indicating that the ocean effect, which is caused by a concentration of electrical currents in the ocean between Africa and Antarctica, is responsible for the anomalous behavior of the C-response. In order to distinguish between real and imaginary parts of the C-response on one plot, the imaginary part is shown with minus sign.

At this stage it is important to remark that the general scheme of IE solution implies that a 3-D model can be excited by any volume extraneous (impressed) current at any location. However, in this section, where the fields and responses generated by the magnetospheric ring current are investigated, the inducing currents are only considered in the form of a spherical harmonic expansion of equivalent sheet currents. These are assumed to flow in a shell at $r = a$ (embedded in an insulator) and to produce exactly the external magnetic field

$$\mathbf{B}^{ext} = -\mathrm{grad}\, V^{ext},\ V^{ext} = a \sum_{n=1}^{\infty} \sum_{m=-n}^{m} \varepsilon_n^m \left(\frac{r}{a}\right)^n P_n^m(\cos\vartheta)\, \mathrm{e}^{im\varphi}, \tag{9}$$

at the Earth' surface $r = a$. In this case the equivalent sheet current $\mathbf{J}_\tau^{ext}$, can be written in the form (Schmucker 1985a, b)

$$\mathbf{J}_\tau^{ext} = \frac{\delta(r-a)}{\mu_0} \sum_{n=1}^{\infty} \sum_{m=-n}^{m} \frac{2n+1}{n+1} \varepsilon_n^m \mathbf{e}_r \times \nabla_\perp (P_n^m(\cos\vartheta)\, \mathrm{e}^{im\varphi}), \tag{10}$$

where $\mathbf{e}_r$ is the outward unit vector, $\times$ denotes a vector product, and $\nabla_\perp$ is the angular part of the gradient. In the case when the model is excited by a large scale, symmetric—with respect to geomagnetic equator—ring current, the sheet current density, $\mathbf{J}_\tau^{ext}$ reduces to

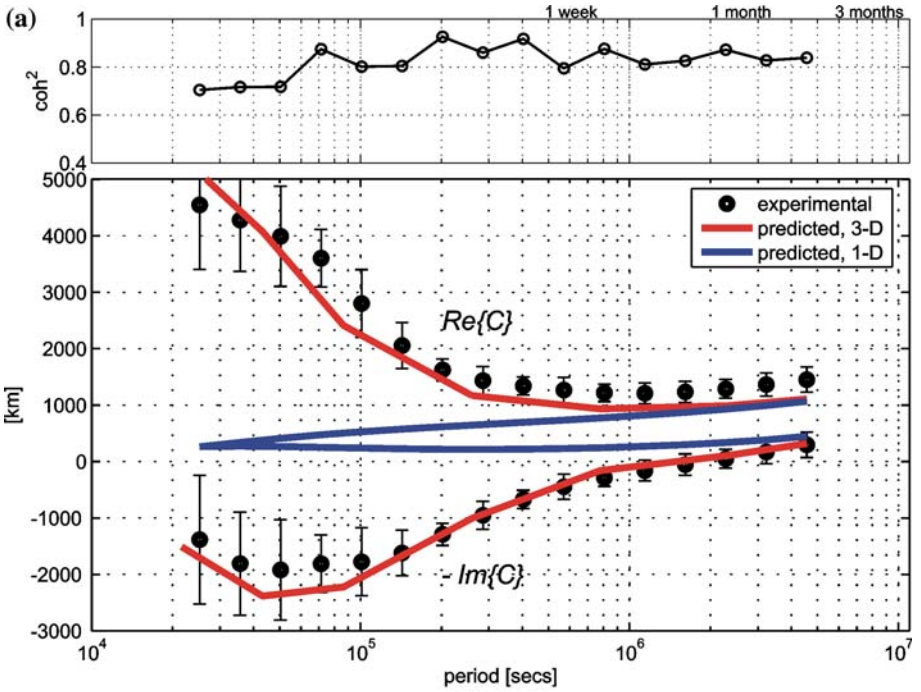
(a)
1 week
1 month
3 months
coh²
1
0.8
0.6
0.4
5000
4000
3000
2000
1000
0
-1000
-2000
-3000
[km]
experimental
predicted, 3-D
predicted, 1-D
Re{C}
Im{C}
10⁴
10⁵
10⁶
10⁷
period [secs]

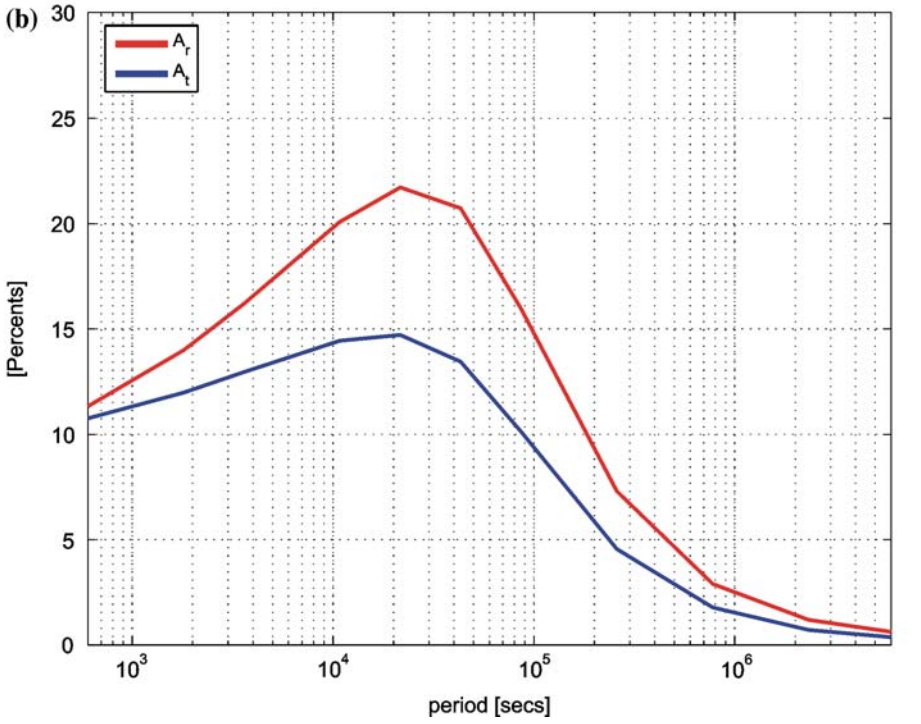
(b)
A_r
A_t
30
25
20
15
10
5
0
[Percents]
10³
10⁴
10⁵
10⁶
period [secs]

◀ **Fig. 4** (**a**) Observed (experimental) and predicted C-responses for the South African observatory Hermanus for 16 periods between 7 h and 52 days. Upper subplot depicts the squared coherency. (**b**) Predicted cumulative (over the globe) estimates of the anomalous effect (in percent) of the oceans in vertical and tangential component (at sea level) for 13 periods between 10 min and 81 days (see Eq. 12)

$$\mathbf{J}_{\tau}^{ext} = -\frac{3}{2}\,\varepsilon_1^0 \sin\vartheta_d \mathbf{e}_{\varphi}\delta(r-a)/\mu_0\,. \tag{11}$$

The lower plot of Fig. 4 shows cumulative (over the globe) estimates, A_r and A_t, of the anomalous effect of the oceans in vertical and tangential component with respect to periods, at sea level. A_r and A_t are defined as

$$A_r = \frac{\int_\Omega |B_r^{3D} - B_r^{1D}|d\Omega}{\int_\Omega |B_r^{ext}|d\Omega} \times 100\%, \qquad A_t = \frac{\int_\Omega |\mathbf{B}_t^{3D} - \mathbf{B}_t^{1D}|d\Omega}{\int_\Omega |\mathbf{B}_t^{ext}|d\Omega} \times 100\%. \tag{12}$$

As expected the size of the anomalous effect is higher in the vertical component. The maximum effect is observed at a period of 6 h. The form of the decay differs when the periods tend to larger or smaller values; the anomalous effect decreases more rapidly as the period increases. Figure 5 demonstrates the global pattern of the anomalous effect in the vertical component at sea level for two periods: 10 min (left hand plots) and 6 h (right hand plots). In what follows, only the vertical magnetic field will be presented, as it is more strongly influenced by induction. Hereafter, the anomalous vertical component, Z^{anom}, is defined as the difference between the fields obtained using the 3-D conductivity model and a 1-D model. Note that the anomalous field contains only the *induced* part of the field, Z^{ind}, that is, $Z^{ind} = Z - Z^{ext}$, since the difference cancels the *inducing* field which is identical for

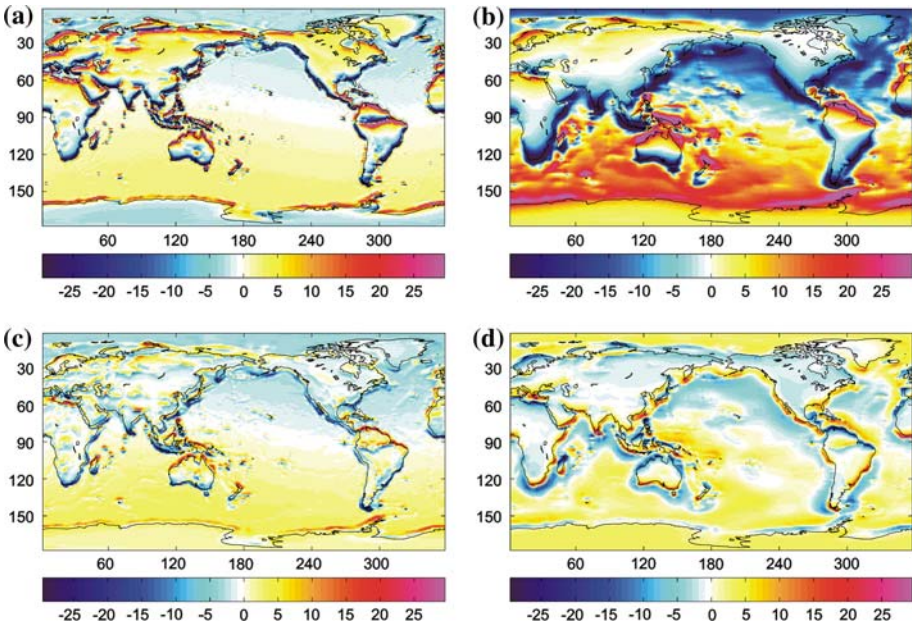

Fig. 5 *Left*: real (**a**) and imaginary (**c**) parts of the anomalous effect in Z (in nT) at sea level for the period of 10 min. *Right*: the same (**b**) and (**c**) but for the period of 6 h. The anomalous effect is defined here as the difference between Z obtained using the 3-D conductivity model (with oceans) and a 1-D model (without oceans)

both the 3-D and 1-D model simulations. i.e., $Z^{anom} = Z^{ext} + Z^{ind,3D} - (Z^{ext} + Z^{ind,1D}) = Z^{ind,3D} - Z^{ind,1D}$. As a consequence of the difference between oceanic and continental values of conductance, there is an anomalous Z in the oceans at a period of 6 h (see Fig. 3). However, the most prominent difference between the 3-D and the 1-D results occurs in coastal regions; for example, it is clearly seen that South Africa is one of the regions where the anomalous effect is substantial. A different global pattern is observed with a period of 10 min. Now the anomalous effect in coastal regions is more spatially concentrated, and moreover has as a whole a different sign in the imaginary part. Also the anomalous effect is now clearly seen on the continents where it closely follows the variability of the inland conductance (cf. Fig. 1b); the most pronounced anomaly inland at a period of 10 min is detected in the Amazon river basin.

Recently Olsen and Kuvshinov (2004) estimated the ocean effect of geomagnetic storms at sea level in the time domain. Their time-domain solution relies on the Fourier transform of frequency-domain calculations. Their results for several major storms show much better agreement between the observed and the simulated magnetic vertical component at coastal sites if the ocean effect is considered.

In independent 3-D modeling studies, Velimsky et al. (2003) and Kuvshinov and Olsen (2005a) demonstrated that induction in oceans considerably influences the magnetic field even at satellite altitudes. Everett et al. (2002) also estimated the anomalous ocean effect from magnetospheric sources at satellite altitudes but in the frequency domain. Figure 6 shows global maps of the total (left hand plot) and anomalous (right hand plot) vertical magnetic field at sea level for one UT instant of the main phase of the storm of 5–6 November 2001. The time-varying magnetospheric source is determined from Oersted, CHAMP and SAC-C satellite data (cf. Kuvshinov and Olsen 2005a). For this and previous examples, the source geometry was approximated by the first zonal harmonic; this geometry is clearly seen in the total Z that is shown in the left hand plots of Fig. 6. Figure 7 presents the anomalous effect in Z at the CHAMP altitude of $h = 400$ km. The ocean effect is here primarily manifested as a sharp field increase near the coasts, reaching some tens of nT during the main phase of the storm, both at sea level (80 nT maximum amplitude) and at the CHAMP altitude (30 nT maximum amplitude).

Figure 8 demonstrates the ocean effect at sea level in more detail. The lower left plot of Fig. 8 presents the time series of observed and modeled Z at selected coastal observatories during the storm of 13–14 July 2000. The source geometry for these simulations is derived

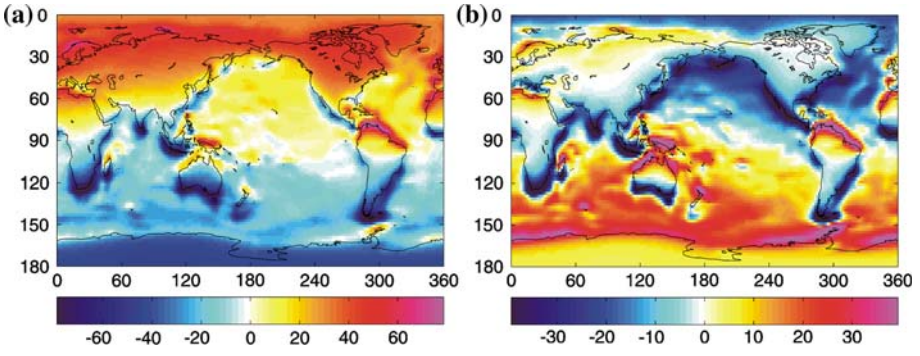

Fig. 6 Global maps of the total (**a**) and anomalous (**b**) Z (in nT) at sea level for one UT instant of the main phase of the storm of 5-6 November 2001. After Kuvshinov (2007)

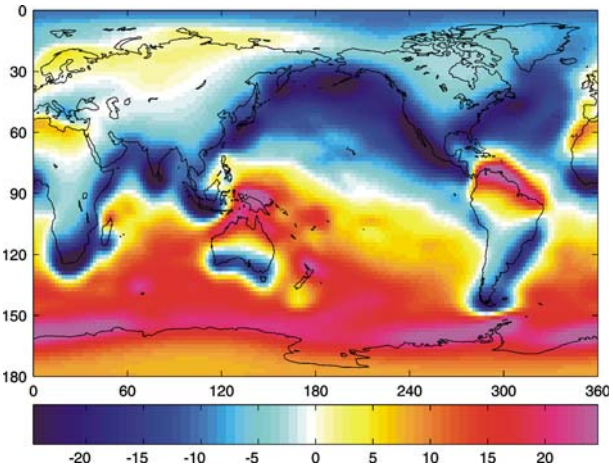

Fig. 7 Global map of the anomalous Z (in nT) at the CHAMP altitude for the same (as on Fig. 5) UT instant of the main phase of the storm of 5–6 November 2001. After Kuvshinov (2007)

from an hour-by-hour spherical harmonic analysis of world-wide distributed observatory hourly mean values (for details see Olsen and Kuvshinov (2004)) and includes the contributions from spherical harmonics up to degree $n = 3$, with the location of observatories used in this study shown in the upper plot of Fig. 8. The results of the 3-D model calculations are shown in red, those of the 1-D model are in blue, and the black lines present the observed data. The green lines show the values based on the *Dst*-index,

$$Z(t) = \varepsilon^0_{1,Dst}(t)(1 - 2\tilde{Q}_1)\cos\vartheta_d, \quad \varepsilon^0_{1,Dst}(t) = -Dst(t)/(1 + \tilde{Q}_1), \tag{13}$$

where $\tilde{Q}_1 = 0.27$ (as determined from satellite data (Langel and Estes 1985)) corresponds to an infinite conductor at 1200 km depth, overlaid by an insulating mantle.

It is seen that there are considerable differences between the 1-D and the 3-D results. The largest difference is found at the South-African observatory Hermanus (HER); the peak of Z during the maximum of the storm is 220 nT for the 3-D case, which is much closer to the observed value (250 nT) than the 1-D result (50 nT). Japanese observatories (KAK, KNY, HTY, KNZ) also show a clear ocean effect, due to their proximity to a deep-sea trench. There is also in this case better agreement between the observations and the model results if the oceans are considered. For comparison, the time series of Z at four inland observatories (ASP, TAM, SUA and KSH) are also shown in Fig. 8. As expected for sites far away from the coast, the 1-D and 3-D results are rather similar. It is also seen from Fig. 8 that, in addition to the induction effects, the contributions from higher harmonics (besides the dominant P^1_0 source) are important (cf. the results based on *Dst*-index which relies on the P^1_0 assumption).

Strictly speaking the anomalous induction near coastlines has at least two possible contributions: the ocean effect, and the conductivity discontinuities in the crust and upper mantle specifically associated with continent-ocean boundaries (for instance, subduction slabs). However, simulations using conductivity models with and without a laterally inhomogeneous lithosphere and upper mantle at the continent-ocean transition indicate that the ocean effect dominates (Kuvshinov et al. 2005).

The lower right plot of Fig. 8 presents the results at Hermanus observatory for major geomagnetic storms. Again only the 3-D results reproduce the observations. The

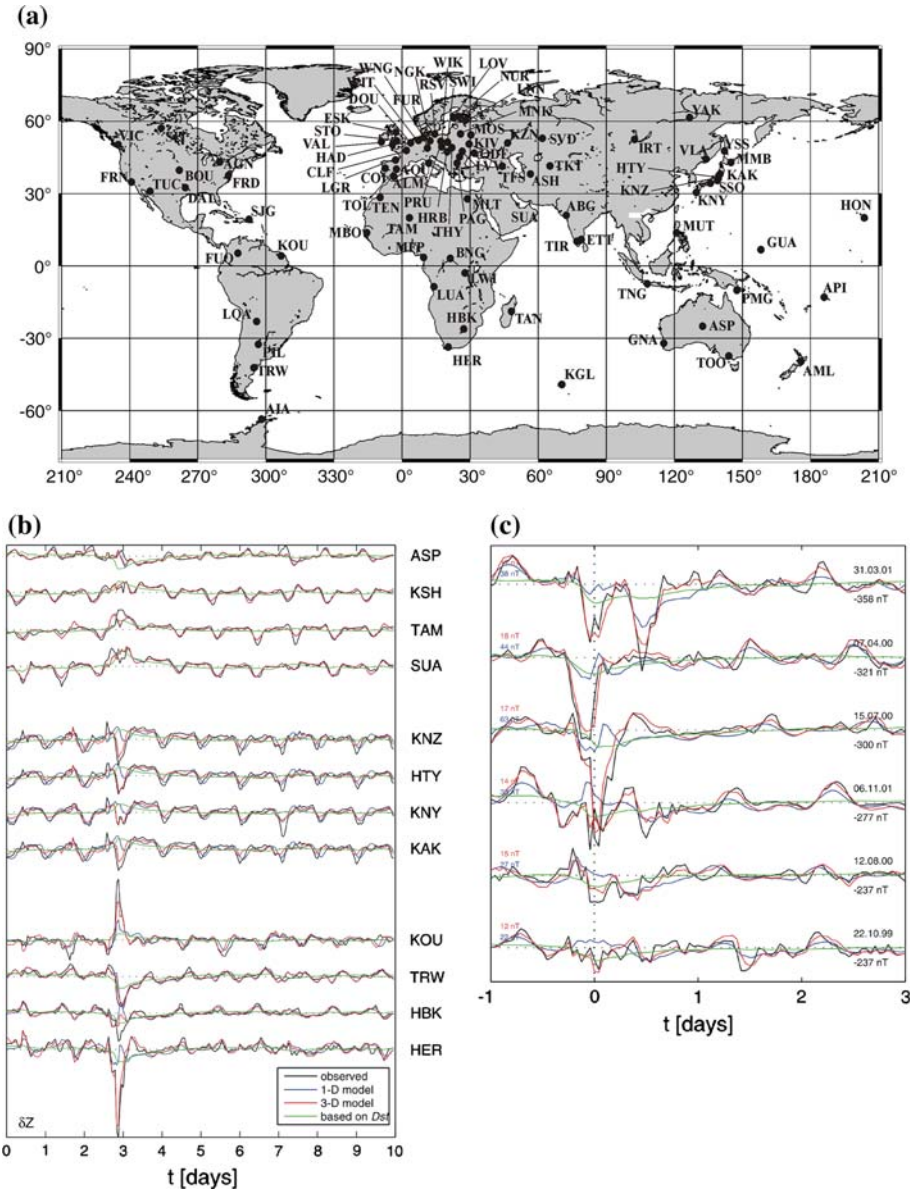

Fig. 8 *Upper*: location of observatories used in this study. *Lower left*: time series of observed and modelled *Z* (in nT) at selected observatories. 3-D model results are shown in red, 1-D results in blue and observed fields in black. The green lines present values based on Dst index. $t = 0$ corresponds to July 13, 2000, 00:00 UT. *Lower right*: time series of observed and modeled *Z* (nT) at Hermanus observatory for selected geomagnetic storms. The numbers at the left of the plot present rms deviations. After Olsen and Kuvshinov (2004)

superiority of the 3-D results is also evident when comparing the root mean square deviation between the observed and predicted *Z*. For example, for the 14 July 2000 storm the differences between observations and predictions based on the 1-D and 3-D models are 63 nT and 17 nT, respectively (cf. the numbers at the left side of Fig. 8).

Calculation of the ocean effect from *Dst* variations has also already been exploited in data analysis and interpretation. Recently, Utada et al. (2003) constructed a new 1-D upper- and mid-mantle conductivity profile beneath the North Pacific Ocean, using a quasi 1-D algorithm to correct the frequency domain responses for the ocean effect. A similar approach has been used by Kuvshinov and Olsen (2006) to correct for the same effect in satellite (induced) geomagnetic signals, but in the time domain.

5 Solar Quiet (Sq) Variations and Equatorial Electrojet (EEJ)

The solar-quiet current system, primarily driven by solar tidal winds in the ionospheric E-layer at an altitude of about 110 km, is spread within a latitudinal limit of ±60°on the sunlit side of the Earth, with an anti-clockwise (clockwise) vortex in the Northern (Southern) hemisphere. The equatorial electrojet is an intense eastward flowing current system in the same ionospheric layer and aligned with the geomagnetic dip equator on the same, sunlit, side of the Earth. The EEJ has a latitudinal width of 6–8 and manifests itself on the ground as more than a threefold increase in the daily variations of the magnetic horizontal component H near the dip equator. Viewed from the Sun, the Earth rotates underneath these ionospheric current systems, and therefore the EEJ and Sq are mainly local time (LT) phenomena. For more information about Sq, see the paper of Schmucker (1999), and concerning the EEJ consult the review by Onwumechili (1997).

Besides the primary effect of ionospheric currents, observations of geomagnetic variations are affected by secondary currents induced in the solid Earth and the oceans. Numerical estimations of the effect of the distribution of resistive continents and conductive oceans on EM induction in the Earth due to Sq currents has been investigated in numerous studies (e.g. Ashour 1965; Bullard and Parker 1970; Hewson-Brown and Kendall 1978; Beamish et al. 1980; Hobbs 1981; Fainberg et al. 1990; Takeda 1991; Velimsky and Everett 2005). Detailed and systematic study of the coast-line effect in Sq variations for surface observatories (and a review of previous work on the subject) can be found in Kuvshinov et al. (1999). Tarits and Grammatica (2000) and Grammatica and Tarits (2002) have qualitatively estimated the influence of near-surface heterogeneities in Sq fields at satellite altitudes.

Electromagnetic induction effects due to the EEJ have been also the subject of many studies (see the detailed reference list in Rastogi (2004)). These have focused primarily on how to explain the geomagnetic daily variations in equatorial regions. A topic of special interest is the anomalous daily variation of Z at South Indian (electrojet) stations. From the geometry of the EEJ current system, one expects negative values of Z at locations North of the dip equator and, additionally, Z should peak around 12:00 LT. Such a behavior of the EEJ was first modeled by Chapman (1951) and matches the observations at most equatorial observatories, but not those in South India. The South Indian observatories (located to the North of the dip equator) show a peak around 9:00 LT, and, moreover, this peak is *positive*. There are many hypotheses about the nature of this anomaly; for a review on the subject see Rastogi (2004). The diversity of hypotheses indicates that there is no agreed explanation of the South India daily variation anomaly so far. One of the complications is that low-latitude EEJ variations are always superimposed on the Sq field and it is still unclear which source is responsible for the anomalies in the daily variations of geomagnetic fields at equatorial latitudes. Kuvshinov et al. (2007) investigated the spatio-temporal behavior of the magnetic vertical component, Z, of the daily ionospheric current systems, Sq and EEJ, considering induction in the mantle and oceans. The inducing EEJ and Sq current systems

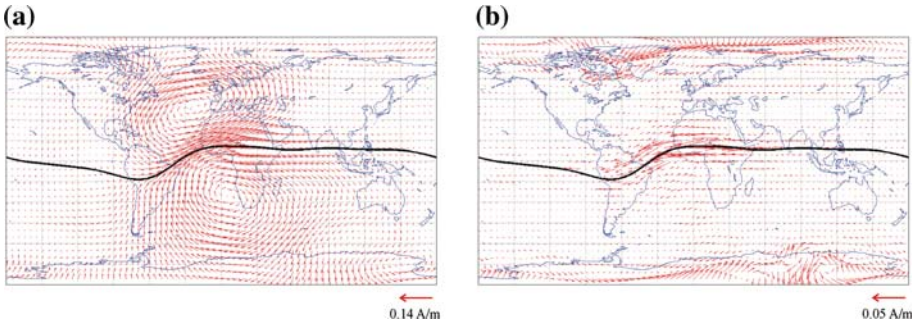

Fig. 9 *Left*: CM4 ionospheric current system (Sq + EEJ), in A/m. *Right*: Small-scale part (EEJ) obtained by spatial high-pass filtering of the current system shown on the left. The sheet currents are for 12:30 UT on 21 March 2000. After Kuvshinov et al. (2007)

are provided by the Comprehensive Model of Sabaka et al. (2004). The 3-D conductivity model of the Earth is described in Sect. 2. Figure 9 shows a snapshot of the Sq (left) and EEJ (right) current systems at 12:30 Universal Time (UT) for a reasonably quiet day during spring conditions (21 March 2000). The location of the dip equator is shown in this and the following figures as a solid black curve. The main features of Sq (two large current vortices which are symmetric around the dip equator) and the EEJ (current concentration near the dip equator) are clearly visible.

Figure 10 presents global maps of the external and induced part of Z calculated at sea level for a fixed local time (LT) of 12:30 for all longitudes, on 21 March 2000. The induced

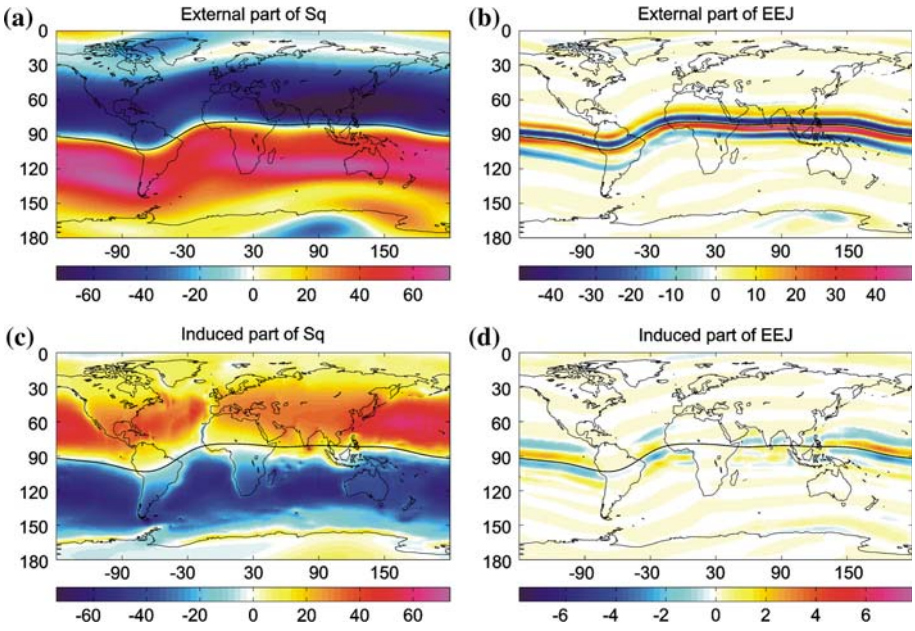

Fig. 10 External (top) and induced (bottom) parts of Z (in nT) due to Sq (left) and EEJ (right) at sea level. The results are for 12:30 LT of 21 March 2000. Note that different scales are used for external and induced fields of the EEJ (right panel). After Kuvshinov et al. (2007)

part, $Z^{ind} = Z^{3D} - Z^{ext}$, is the difference between the total field Z^{3D} (calculated using the 3-D conductivity model) and the external field, Z^{ext}. Results for Sq are shown in the left hand plots; those for EEJ are shown in the right hand plots. The external signals (primary magnetic signals from the ionospheric current systems) reflect the structure of the corresponding ionospheric current systems. For example, Z^{ext} of the EEJ reveals four stripes of alternating signs that follow the dip equator and agree with the geometry of the EEJ currents—a dominant eastward current and weaker return currents to the North and South of the dip equator. The four-stripe structure is most distinctly resolved in the Eastern Pacific region for this local time.

As expected, the induced signals in Z at the ground have opposite sign compared with the external signal. The induced signal of Sq is of the same order of magnitude as the external signal, reaching 80% of the external in the Northern Pacific region. In general, the induced signals over the continents are smaller than those over the oceans both for Sq and EEJ. Moreover, the induced signals of the EEJ are negligible (well below 0.5 nT) inland, including coastal regions. They comprise less than 1% of the maximum external signal, which has an amplitude of about 50 nT at the dip equator for this particular day. The negligible amplitude of the induced signals from the EEJ everywhere inland is in agreement with theoretical estimates (presented in Fig. 3) of the induced/external ratio, $Q_n{}^r$, for a 1-D mantle conductivity model without oceans, due to the small spatial scale of the primary EEJ current system which is described by spherical harmonics of $n \geq 180^\circ/8^\circ = 22$ (here 8° is the upper bound on the estimate of the EEJ width). 1-D conductivity models, however, do not completely explain the spatio-temporal behavior of Z because the distribution of resistive continents and conductive oceans is nonuniform. Figure 11 presents global maps of the anomalous Z for three LT instants (9:30, 12:30 and 15:30) of the same day.

Results for Sq are presented in the left hand plots of Fig. 11. As in the case of the magnetospheric source, the most prominent differences between the 3-D and the 1-D results occur in coastal regions. The intensity and sign of these coastal anomalies vary with local time and demonstrate a different behavior in different regions of the world. For example, there exist large signals of opposite sign around 09:30 and 15:30 LT on the Western and Eastern coasts of Australia, but this anomalous effect is rather small at 12:30 LT. Such an anomaly is also observed along the North-Western coast of Africa where the effect is large at local noon but almost absent at 09:30 and 15:30 LT. Regions with clearly visible anomalous effects near the dip equator include South India and Sri Lanka. Unlike many other coastal regions, this anomaly is present at all investigated local times.

It is interesting that for many regions of the world the geometry of the coastal effect in Sq signals differs significantly from that in magnetospheric signals. For example, the coastal effect from the magnetospheric source is most prominent on the Northern and Southern coasts of Australia, whereas the effect for a Sq source is much larger on the Western and Eastern coasts (cf. Figs. 6b and 11a). A similar situation occurs in South Africa. Evidently this is due to the different spatial structure of these two sources.

The right hand plots of Fig. 11 show results for the EEJ. There are at least three differences compared with Sq: (a) induction from the EEJ is confined to oceanic regions, (b) maximum induction signals occur before and after noon, and (c) no coastal anomalies are generated at any of the local times considered.

Figure 12 presents estimates of the anomalous induction from Sq at local midnight, since satellite data around local midnight are used to determine the core and lithospheric field. It is assumed that non-polar ionospheric signals are very weak during the night, if not absent. An anomalous Z value is presented for 23:30 LT at sea level and also at the CHAMP satellite altitude of 400 km. At sea level, the anomalous signals at midnight reach

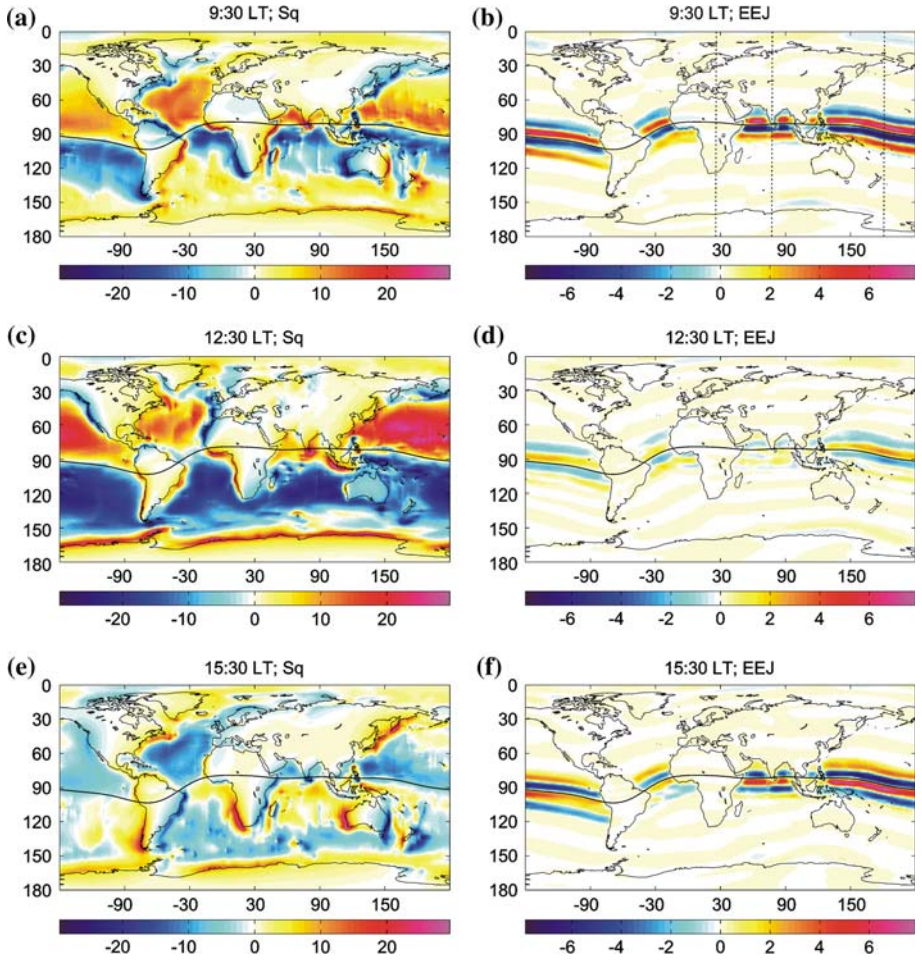

Fig. 11 Anomalous Z (in nT) due to Sq (left) and EEJ (right) at sea level for three local time instants on 21 March 2000: 09:30 LT (top), 12:30 LT (center) and 15:30 LT (bottom). After Kuvshinov et al. (2007)

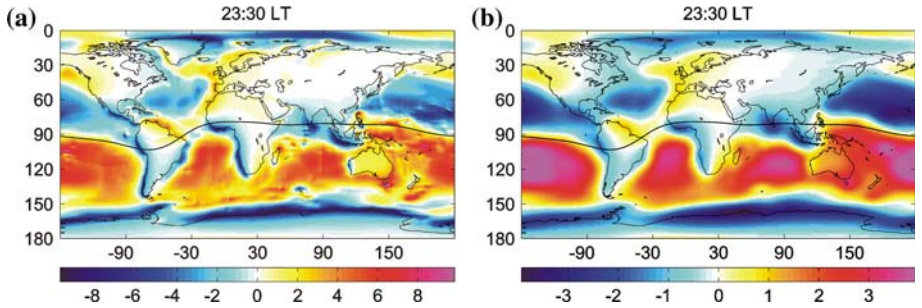

Fig. 12 Anomalous Z (in nT) due to Sq at 23:30 LT on 21 March 2000 at sea level (left) and the CHAMP altitude of 400 km (right). After Kuvshinov et al. (2007)

6–8 nT in many coastal regions (say, in South India and Indonesia) and have a small-scale spatial structure similar to the lithospheric field (and therefore can be erroneously attributed to it). At satellite altitudes the anomalous Sq signals are much smoother but still visible, with amplitudes of 2–4 nT. The latter result agrees with the estimates of the Sq ocean effect at satellite altitudes presented by Grammatica and Tarits (2002).

The model results presented here are based on the ionospheric currents as provided by the CM4 model. However, this model is an approximation of the actual ionospheric currents. In particular, CM4 was derived assuming a 1-D electrical conductivity model of the Earth (cf. Sabaka et al. 2004). As a consequence, ocean induction effects are ignored. As CM4 is based not only on observatory data but also on satellite data, this assumption affects the determination of the ionospheric currents, as satellites pass over both continents and oceans. To illustrate the possible amount of distortion, Fig. 13 presents global maps of 1-D Z (left) and anomalous Z (right) due to Sq for 12:30 LT at CHAMP altitude. The anomalous (ocean) effect at 400 km altitude is smoother and weaker compared to the ground results (cf. Fig. 11c) but still reaches 15 nT in oceanic regions, which amounts to 50% of the total 1-D signal. Thus, assuming a 1-D conductivity model can introduce serious errors in the determination of ionospheric current systems.

Figure 14 compares our predictions with data from two Indian electrojet observatories, where an anomalous behavior of Z (*positive* pre-noon peak, instead of (normal) *negative*

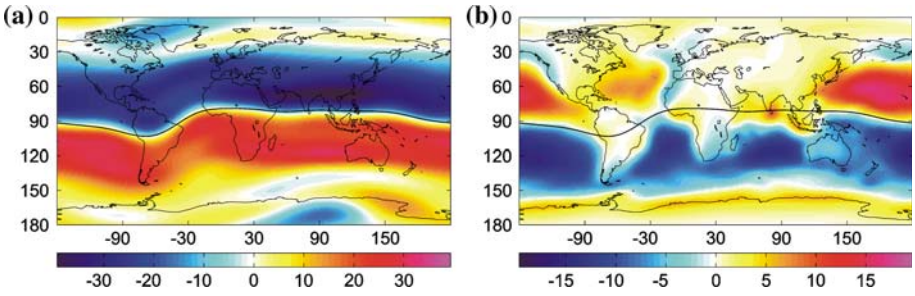

Fig. 13 Z (in nT) predicted by a 1-D model (left), and anomalous Z (right), due to Sq for 12:30 LT on 21 March 2000 and altitude of 400 km. After Kuvshinov et al. (2007)

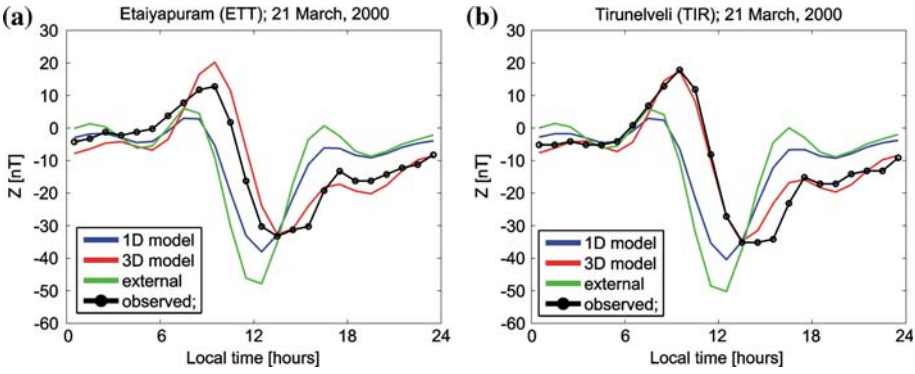

Fig. 14 Observed (black) and predicted daily variations of Z (in nT) as a function of local time on 21 March 2000 for the South Indian observatories Etaiyapuram (left) and Tirunelveli (right). After Kuvshinov et al. (2007)

noon peak) has been found. Figure 14 presents the predicted and observed daily variations as a function of local time on 21 March 2000. There is remarkable agreement between the observations and the 3-D predictions. The results show that the anomalous variations in Z are due to 3-D induction in the oceans. Figure 15 shows that the Sq, and not the EEJ, is responsible for the observed anomaly. The left and right hand plots of Fig. 15 show predicted results for Sq and for the EEJ at the observatory Tirunelveli (TIR). As expected, induction by the EEJ is negligible at the electrojet sites in India, and the anomalous behavior of Z is fully accounted for by 3-D induction of Sq variations.

Figure 16 presents a comparison of the daily variation of Z at two mid-latitude observatories, Moscow (MOS) and Memambetsu (MMB). The Russian observatory Moscow is located far inland and hence there is no anomalous induction. However, the Japanese observatory Memambetsu, located on the coast near a deep ocean trench, is strongly affected by the ocean effect. But, in contrast to the South Indian sites, the ocean effect at MMB shows up in a different way, namely as a 2 h shift of the local noontime peak towards the morning hours.

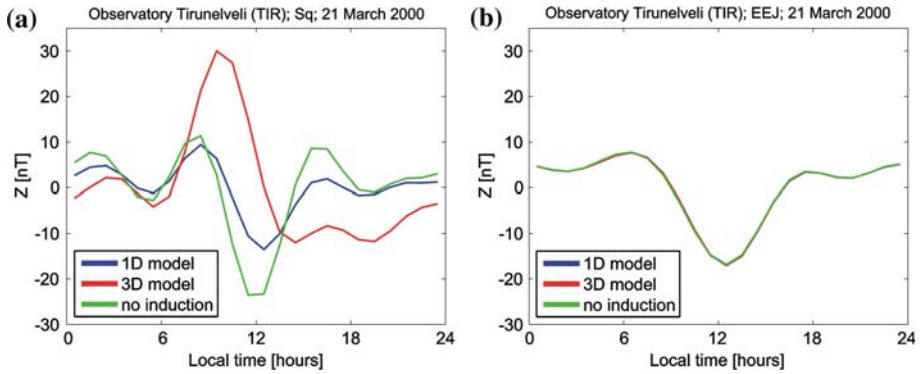

Fig. 15 Predicted daily variations of Z due to Sq (left) and EEJ (right) on 21 March 2000, for the South Indian observatory Tirunelveli. Note that some profiles in the right panel are almost identical and therefore not visible. After Kuvshinov et al. (2007)

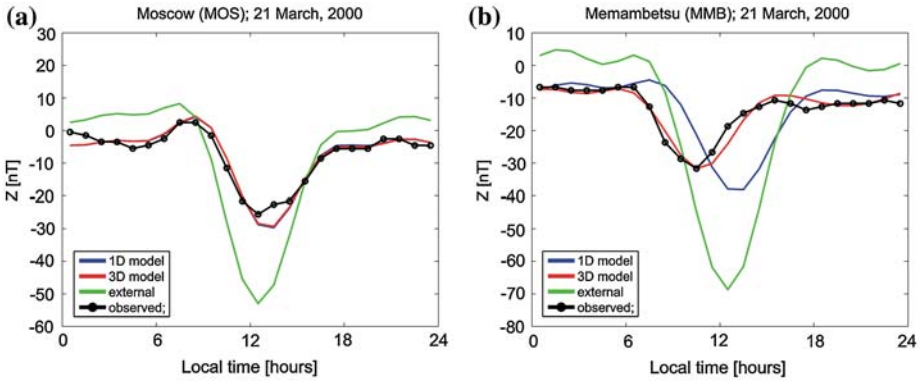

Fig. 16 Observed (black) and predicted daily variations of Z on 21 March 2000, for the Russian observatory Moscow (left) and the Japanese observatory Memambetsu (right). After Kuvshinov et al. (2007)

To conclude this section we would draw attention to the following issue. Traditionally the ocean effect is considered as an undesirable factor that distorts 1-D results. But one can look at the ocean effect in a more positive way. It is well-known that most of existing estimates of global distributions of deep conductivity are restricted to a depth of more than 200–300 km. One reason for this is that the final interpretation is performed within the framework of 1-D conductivity models, and thus only the induction mode of the electromagnetic field is considered. This has the consequence that shallower, more resistive (lithospheric), layers cannot be resolved since the induction mode is only weakly sensitive to poor conductors (cf. Fainberg et al. 1990).

The situation changes if a model which consists of 1-D mantle conductivity, overlaid by inhomogeneous oceans of known conductance, is considered. Fainberg et al. (1990) and, later, Kuvshinov et al. (1999) clearly demonstrate that, if such a model is exploited, the changes of lithospheric resistivity produce observable changes in the vertical magnetic field variations of both magnetospheric or/and ionospheric origin, near coastlines. This is due to the fact that now the galvanic mode—responsible for the vertical electric currents—enters into the solution near the coastlines, providing the desired sensitivity with respect to the high resistivities of upper layers. Kuvshinov et al. (1999) show that on average a two order of magnitude change in resistance of the lithosphere leads to one order of magnitude change in the coastal Z signal. They also obtain, using the Sq data from 12 coastal observatories, a global estimate (of order of magnitude $10^9\ \Omega\ m^2$) for lithospheric resistance.

6 Polar Electrojets

At least two types of ionospheric currents flowing at high geomagnetic latitudes can be distinguished: these are the substorm electrojet and convection electrojet (cf. Baumjohann and Treumann 1996). The substorm electrojet is characterised by large and rapid temporal changes, and strong spatial inhomogeneity (e.g. Pulkkinen et al. 2003). Pulkkinen and Engels (2005) performed model studies for the Scandinavian region to study the effect of 3-D induction in the Earth on estimates of ionospheric equivalent currents of the substorm electrojet over Scandinavia.

Here 3-D induction effects in the magnetic field produced by the convection electrojet for both the North and South polar caps are reported. A model of the source that resembles reality as closely as possible is constructed; the ionospheric equivalent current system consists of two semiovals on the day and night sides in magnetic local time (MLT); see the left hand plot of Fig. 17. The axis of symmetry is the 11/23 MLT line, consistent with observations (Wang et al. 2005). The right hand plot of Fig. 17 shows the adopted current profile across the ovals. The current system is placed at an altitude of 110 km, with maximum amplitudes at 20 degrees away from the magnetic poles. It is assumed that this current system rotates around the magnetic poles following the Sun. Figure 18 shows the external (inducing) vertical component of the South polar electrojet at sea level for midnight UT.

The left hand plots in Fig. 19 demonstrate 3-D internal (induced) signal for the North (upper plots) and South (lower plots) polar regions. The results are for midnight (UT) at sea level. The right hand plots show the conductivity distribution in the region. It is seen that the internal signal is mostly confined to oceanic regions, with some signal also at coasts and inland. As expected, there is a time lag between inducing and induced signals (cf. Figs. 18 and 19c). One can also see that the induction signal is substantially larger in the South polar region due to a larger amount of deep ocean beneath the convection electrojet.

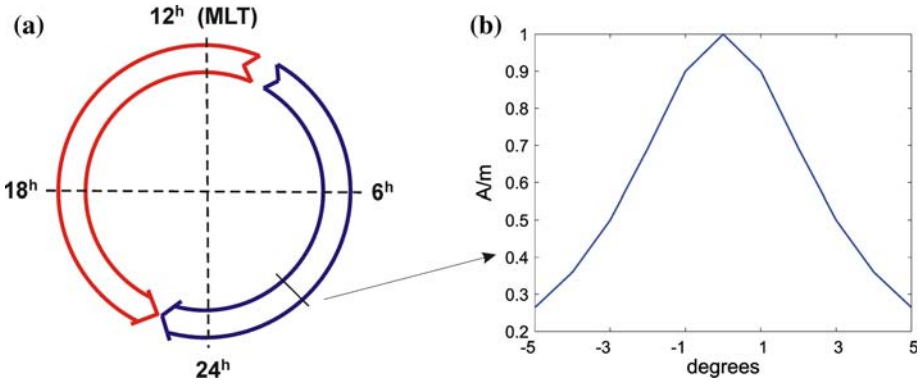

Fig. 17 Model of the polar convection electrojet. *Left*: the geometry of ionospheric equivalent current system. The axis of symmetry is the 11/23 MLT line. *Right*: adopted current profile across the ovals. The current system is placed at altitude of 110 km, with maximum amplitudes on 20 degrees away from the magnetic pole. We assume that this current system rotates around magnetic poles following the Sun

For a comparison, Fig. 20 shows the predictions of the induced signal in the South pole region (at sea level and for midnight) using two 1-D models. The left hand plot shows the result for a model with a perfect conductor at 250 km depth. Note that a model with a perfect conductor is often used to account for induction in satellite and ground-based studies of ionospheric sources. The right hand plot shows the results for a realistic 1-D mantle without oceans. It is seen that the results for the 3-D Earth are quite different from those for the 1-D Earth (cf. Fig. 19c). The model with the perfect conductor gives a higher signal compared with the 3-D results, and predicts a different spatio-temporal behavior involving no time lag, and with the amplitudes of the internal signal exactly following the external signal. The results for the realistic 1-D mantle conductivity model are close in geometry to the 3-D results but much smaller in amplitude. Small differences in the morphologies can be explained by the fact that the source considered is narrow and thus no strong anomalous behavior at the ocean-continent contacts is expected, by analogy with the EEJ fields. In general, 3-D results give larger amplitudes for the internal field compared to the 1-D case, since the source is, to a large extent, located above ocean regions.

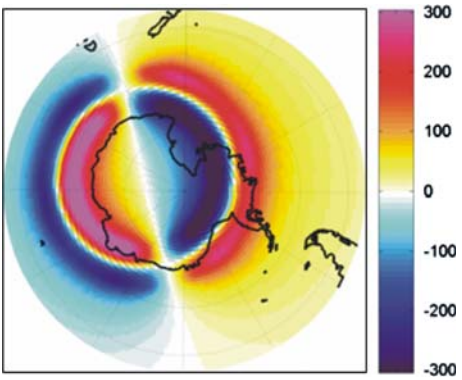

Fig. 18 External (inducing) vertical component (in nT) of the South polar convection electrojet at sea level for midnight UT

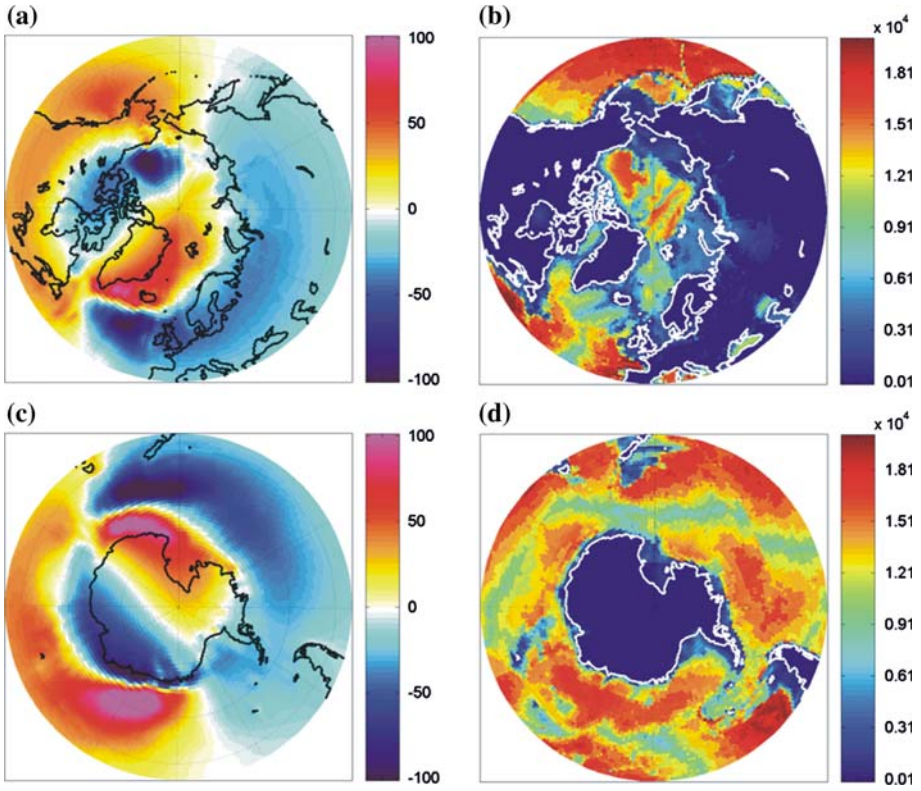

Fig. 19 *Left*: Internal (induced) vertical component (in nT) for North (upper plot) and South (lower) polar regions, calculated in 3-D model. The results are for midnight UT at sea level. *Right*: conductance distribution in these regions (in S)

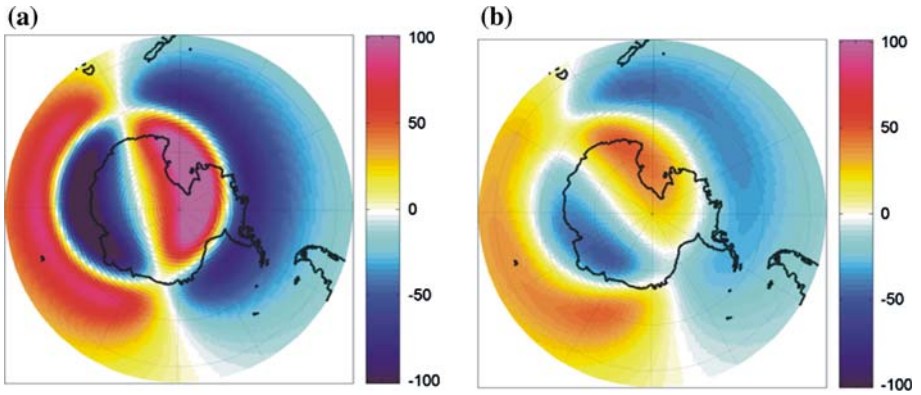

Fig. 20 Internal (induced) vertical components (in nT) for South polar region, calculated in two 1-D models. The results are for midnight UT at sea level. *Left*: The results for 1-D insulating mantle with perfect conductor at 250 km depth. *Right*: The results for a realistic 1-D mantle

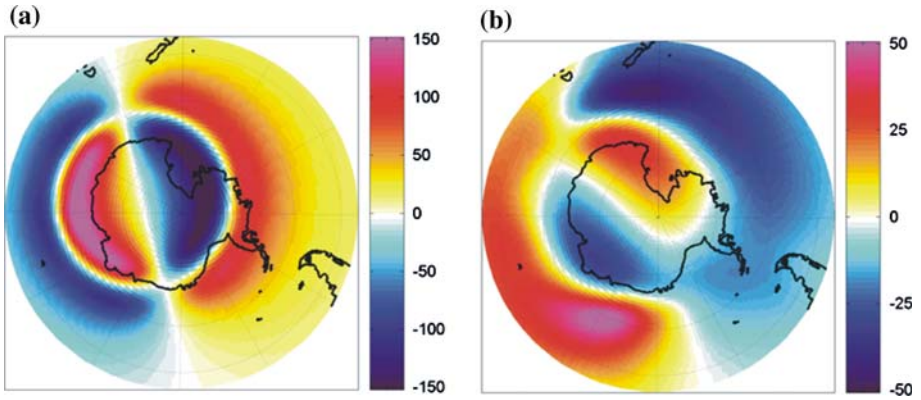

Fig. 21 External (*left*) and internal (*right*) vertical components (in nT) for South polar region. The results are for midnight UT at the CHAMP altitude

Figure 21 shows predictions due to the polar convection electrojet at the CHAMP altitude, again for the South polar region, and for midnight. The left hand plot displays the external signals, with the induced signals being shown on the right. Even at the CHAMP altitude, the induced signal from the polar electrojet is substantial and reaches one third of the external signal. It is interesting that the intensity of the induced signal varies with magnetic local time. It is a minimum at afternoon and post-midnight times MLT, and a maximum at pre-noon and pre-midnight times (MLT).

7 Ocean Tides

Another source of magnetic signals originating in the oceans is motionally-induced electric currents. As electrically conducting water in the oceans moves through the ambient magnetic field of the Earth, it induces secondary electric and magnetic fields. In the last few years much attention has been given to the periodic magnetic signals caused by lunar tidal ocean flows. Tyler et al. (2003) demonstrated that the magnetic fields generated by the lunar semidiurnal M2 (of 12.42 h period) ocean flow are clearly identified in satellite magnetic observations. They compared their numerical simulations of magnetic fields due to the M2 tide with CHAMP observations and found quite close agreement between the observations and predictions (see Fig. 22). Their conductivity model consists of a surface thin shell and an insulating mantle underneath. The discrepancy between observations and predictions has been attributed to the absence of coupling between the surface shell and a conducting mantle.

Maus and Kuvshinov (2004) and Kuvshinov and Olsen (2005b) performed model studies and derived the magnetic signals of various tidal constituents in the presence of a conducting mantle. Note that for these "tidal" simulations the extraneous current $\mathbf{j}^{ext}$ in equations (1) simplifies to the sheet current density, $\mathbf{J}_\tau^{ext}$, which is calculated as

$$\mathbf{J}_\tau^{ext} = \sigma_w(\mathbf{U} \times \mathbf{e}_r B_r^m), \tag{14}$$

where $\mathbf{U}$ is the depth integrated tidal velocity (transport), taken from the TPXO6.1 global tidal model of Erofeeva and Egbert (2002), $\mathbf{e}_r$ is the outward unit vector and B_r^m is the

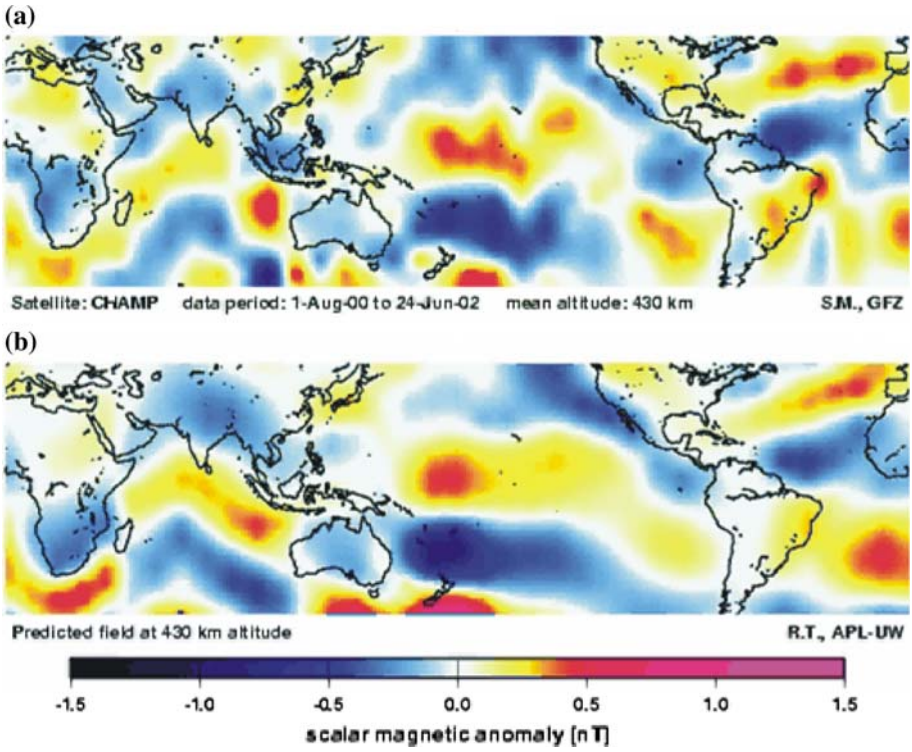

Fig. 22 High pass filtered CHAMP (**a**) and predicted (**b**) in-phase (real) part of scalarmagnetic field due to the periodic M2 tide. From Tyler et al. (2003)

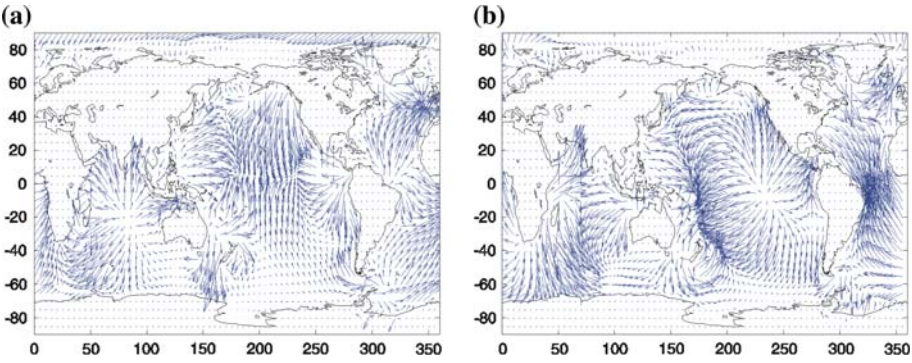

Fig. 23 Depth integrated velocities (in m^2/s), **U**, of the M2 tide. Right and left panels are real and imaginary parts of **U**, respectively. Maximum arrow length is 240 m^2/s

radial component of the main magnetic field derived from the model of Olsen (2002). Figure 23 presents global maps of real (left) and imaginary (right) parts of **U** due to the M2 tide. Figure 24 shows the radial component of the main magnetic field, B_r^m, at the surface of the Earth. Figure 25 presents global maps of the predicted real (left hand plots) and imaginary (right hand plots) parts of the vertical component of the magnetic fields due to

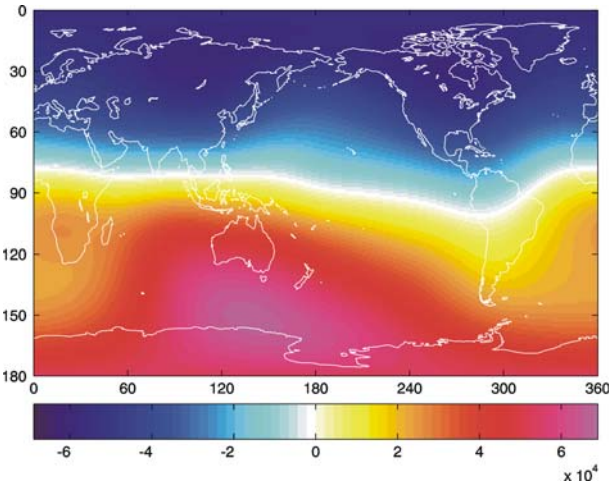

Fig. 24 B_r^m component of the main magnetic field (in nT) at the Earth's surface

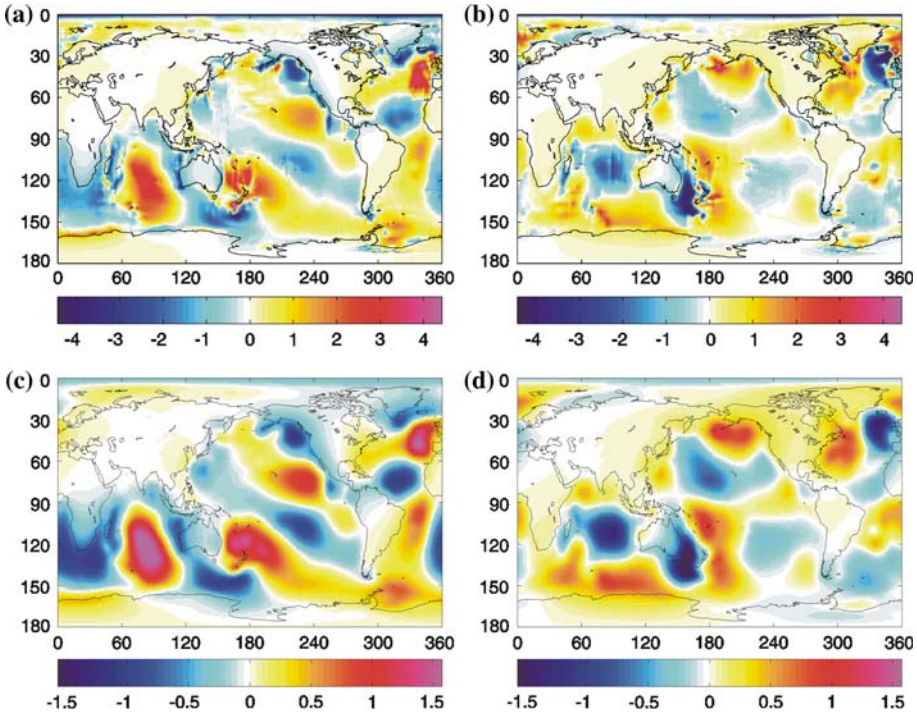

Fig. 25 Z (in nT) due to the M2 tide at sea level (upper plots) and at the CHAMP altitude (lower plots). Right and left plots are in-phase and quadrature parts of Z, respectively. After Kuvshinov and Olsen (2005b)

the M2 tide at sea level (upper plots) and at the CHAMP altitude (lower plots). For comparison, Fig. 26 shows the O1 tide (25.82 h period) magnetic signal at the CHAMP altitude. These two tides are presented, since they are well known as the dominant tidal

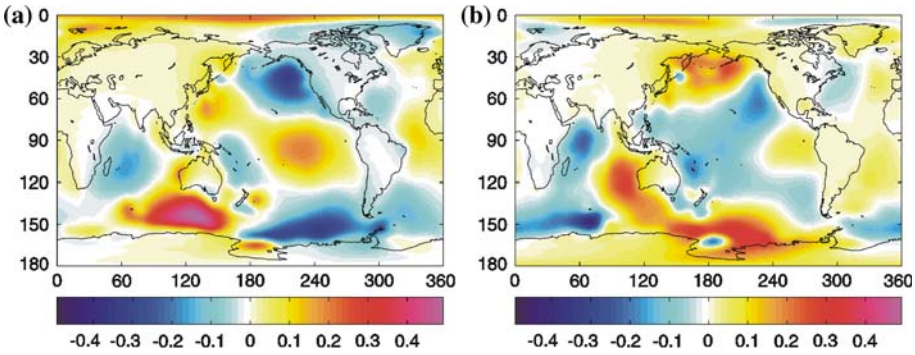

Fig. 26 *Z* (in nT) due to O1 tide at the CHAMP altitude. Right and left panels are in-phase and quadrature parts of *Z*, respectively. After Kuvshinov and Olsen (2005b)

signals produced by the oceans. In accordance with the geometry of the exciting current, which, in particular, is governed by the radial component of the main magnetic field (cf. Fig. 24 and Eq. 14), the signals are negligible at the dip equator and increase towards the magnetic poles. Also, the maxima of the magnetic field amplitudes follow those of the depth-integrated velocities, as expected.

The largest amplitudes of the M2 tidal magnetic field (about 5 nT at sea level) occur in the Indian Ocean, the western part of the South Pacific Ocean, the North Pacific Ocean and the North Atlantic Ocean. The magnitude at the CHAMP altitude decreases, down to 2 nT, and its spatial morphology is smoother compared with that at sea level. The magnetic signals of the O1 tide are at least a factor of three smaller compared to M2 and have a quite different geometry. The largest amplitudes are observed in the North Pacific Ocean and in the region between Australia and Antarctica. Simulations of the magnetic signals due to the other tidal constituents (S2, N2, K2, K1, P1, Q1, MM, MF) have revealed that their strength is also much smaller than for M2. The upper plot of Fig. 27 presents the mean square magnetic field strength with respect to degree, *n*, derived from our predictions of all periodic tides. Evidently the M2 signal prevails but, as was shown by Maus et al. (2006), by accumulating the predicted results from all tidal components it is possible to suppress tidal noise in the CHAMP magnetic observations. The lower plot of Fig. 27 illustrates this fact. Here the black and red curves are spectra of the magnetic residuals over the Indian Ocean before and after subtracting tidal predictions from all major tidal constituents.

Finally, Fig. 28 shows the amplitudes of the high-pass filtered modeled and observed magnetic M2 scalar anomaly, averaged over all latitudes between $-60°$ and $+60°$, illustrating the dependence on longitude. Results are shown for different mantle conductivity models beneath the surface shell. For the "nonuniform lithosphere" model, the resistivity of the uppermost 100 km is set to 300 Ωm beneath the oceans, whereas that beneath the continents is set to 3000 Ωm. The largest difference in the magnetic field at the CHAMP altitude is found when comparing the results for an insulating mantle with those for a realistic (conducting) mantle. This, in particular, means that considering a conducting mantle yields significant changes of the M2 magnetic signals. It is seen that the predictions with a conducting mantle are closer to the observations, though discrepancies are still clearly visible.

Along with the detection of tidal signals in the magnetic field, many authors (cf. Rooney 1938; Harvey et al. 1977; Junge 1988) observed tidal signals in the inland electric field.

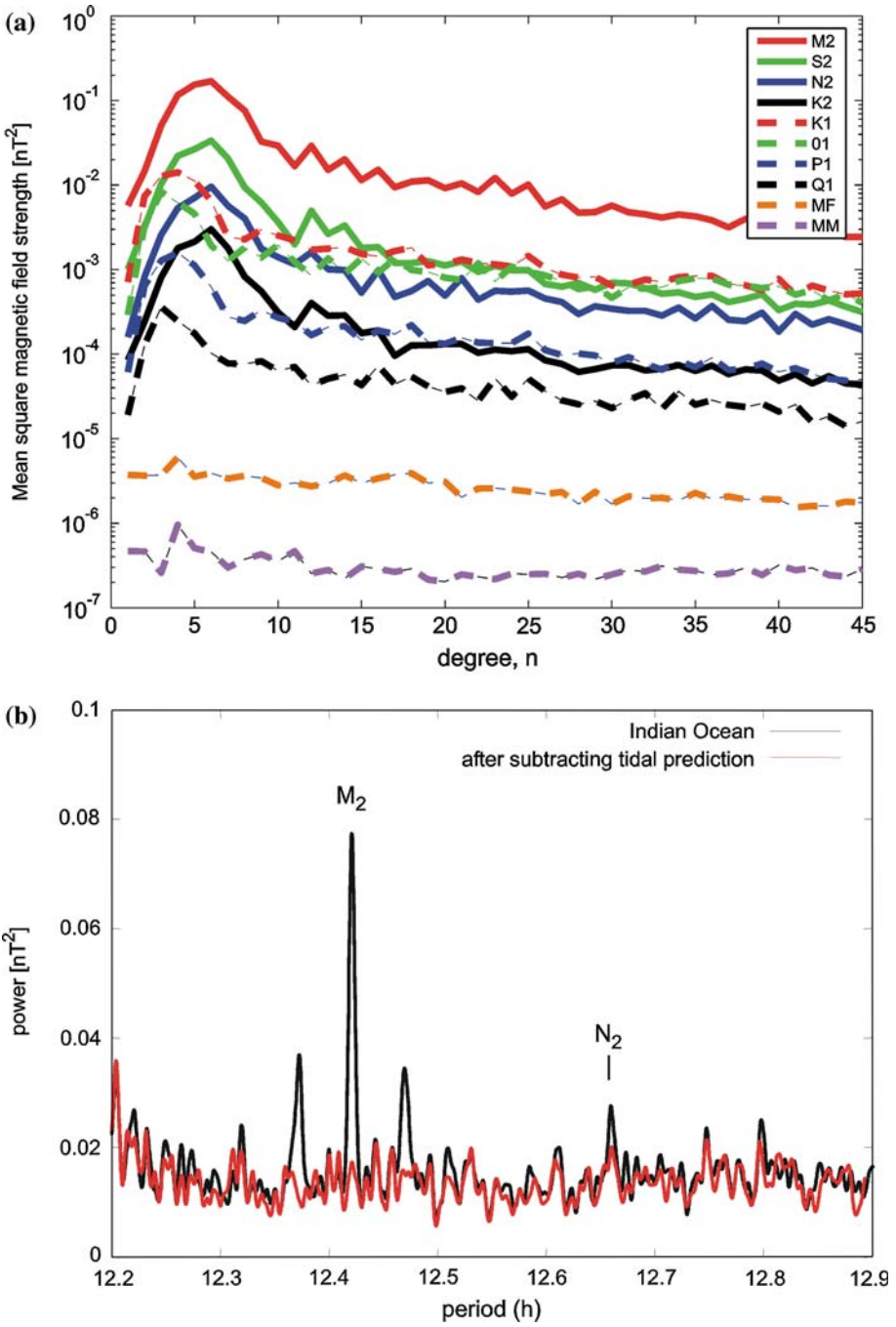

Fig. 27 *Top*: Mean square magnetic field strength with respect to degree, *n*, derived from predictions of all periodic tidal constituents. *Bottom*: Black and red curves are spectra of magnetic residuals over the Indian Ocean before and after subtracting predictions from all major tidal constituents (after Maus et al. 2006)

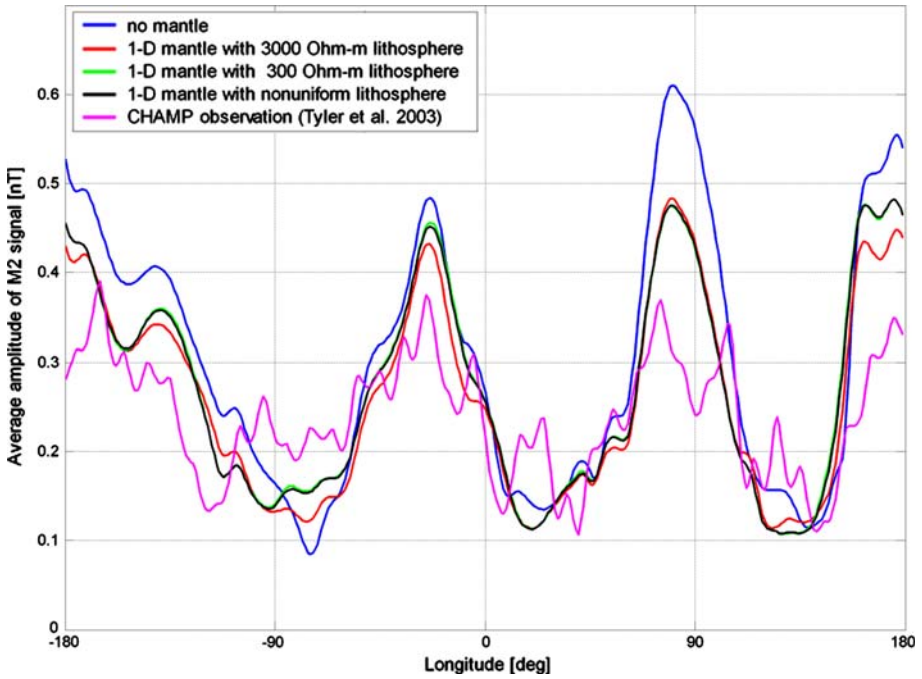

Fig. 28 Meridionally averaged magnetic signal amplitudes (nT) at the CHAMP altitude, calculated for various mantle conductivity models (which are overlaid by surface nonuniform shell). Also shown are observational results, obtained from CHAMP scalar data by Tyler et al. (2003). After Kuvshinov and Olsen (2005b)

These signals are also identified in the voltages that are measured with the use of submarine cables (cf. Duffus and Fowler 1974; Fujii and Utada 2000). So far, the work on this has been limited to experimental observations of the phenomena and no quantitative prediction of the tidal electric fields has been made. Recently Kuvshinov et al. (2006b) performed simulations in order to: (1) understand the global pattern of the electric fields due to M2 and O1 tides, (2) investigate the dependence of the tidal electric field and cable voltages on the changes of lithospheric resistance, $R = \rho h$, where ρ and h are, respectively, the resistivity and the thickness (adopted as 100 km) of the lithosphere, and (3) compare the predictions with existing experimental results.

Figure 29 presents the electric fields due to the O1 and M2 tides for $R = 10^9\ \Omega\ \mathrm{m}^2$. It is seen that sharp contrasts in surface conductance produce abrupt enhancements of electric fields on the coasts. The largest amplitudes of the O1 tide electric field (about 10 mV/km) are predicted at the coast of Antarctica, while the maximum amplitudes of the M2 tide field (about 100 mV/km) are predicted on the North-East coast of Canada. Apart from these regions, there are also many coastal regions where one expects to detect tidal electric field signals. As an example, for the M2 tide these regions are northern Europe, Japan, the western coast of North America, New Zealand, and the coastal zones of Australia and South Africa.

Figure 30 presents the M2 tidal electric field for the model with a less resistive lithosphere ($R = 10^7\ \Omega\ \mathrm{m}^2$). Comparison with the results for a model with a more resistive lithosphere (cf. Fig. 29, bottom plots) supports a significant feature of the motionally-

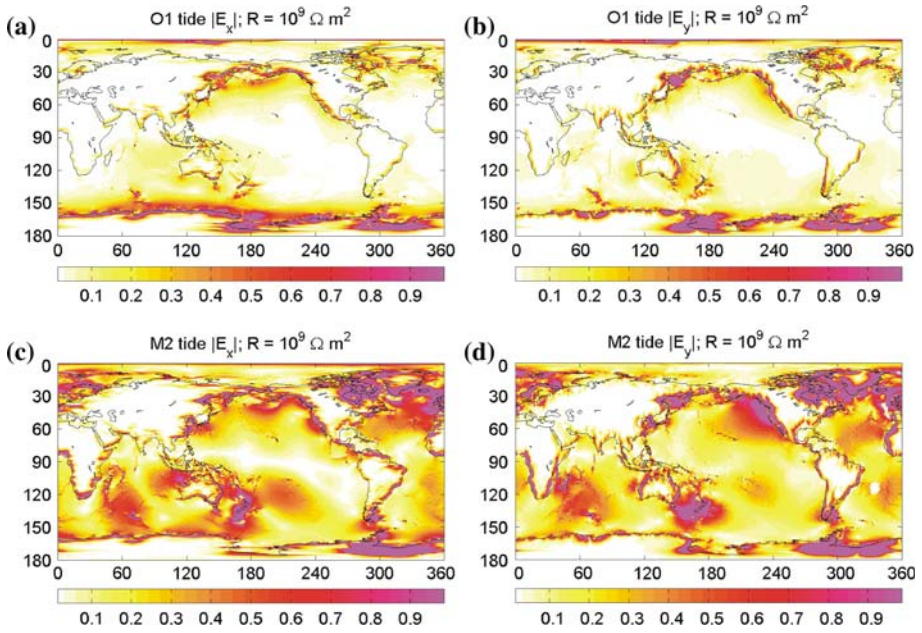

Fig. 29 *Upper*: Magnitudes of electric field components E_x (left) and E_y (right) due to O1 tide. *Lower*: Magnitudes of electric field components E_x (left) and E_y (right) due to the M2 tide. The results are for $R = 10^9\ \Omega\ \mathrm{m}^2$. After Kuvshinov et al. (2006b)

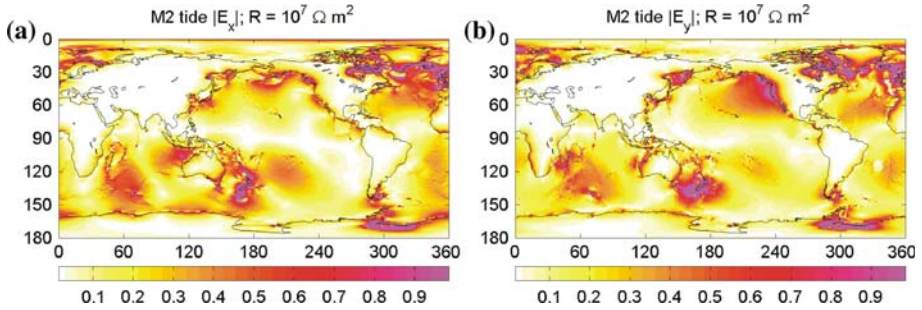

Fig. 30 Magnitudes of electric field components E_x (left) and E_y (right) due to M2 tide. The results are for $R = 10^7\ \Omega\mathrm{m}^2$. After Kuvshinov et al. (2006b)

induced electric field (cf. Palshin et al. 1999)—its dependence on R. The model with a more resistive lithosphere shows coastal anomalies which are much more prominent in amplitude and decay at larger distances inland, as a result of a smaller leakage effect. Figure 31 illustrates the tidal electric field dependence on R in more detail. It presents, for a few values of R, the M2 tidal electric signal along the profile that crosses South Africa. The coastal tidal signal varies here from 0.5 mV/km for $R = 10^7\ \Omega\ \mathrm{m}^2$ to 4 mV/km for $R = 10^9\ \Omega\ \mathrm{m}^2$.

Figure 33 presents the comparison between our predictions and tidal M2 electric signals observed by Junge (1988) at four sites in northern Germany (see their location on Fig. 32, left hand plot). Figure 34 demonstrates, in a similar manner, the comparison between

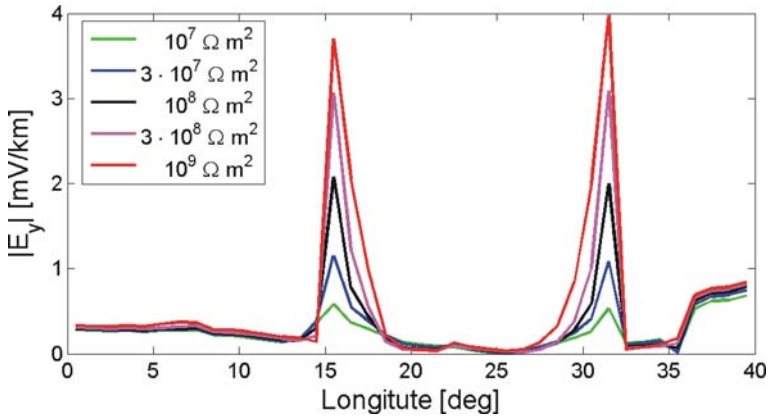

Fig. 31 Amplitudes of the M2 tide E_y along 30° S profile that crosses South Africa, for different values of R. The longitudinal location of the coasts are 15.5° E and 31.5° E. After Kuvshinov et al. (2006b)

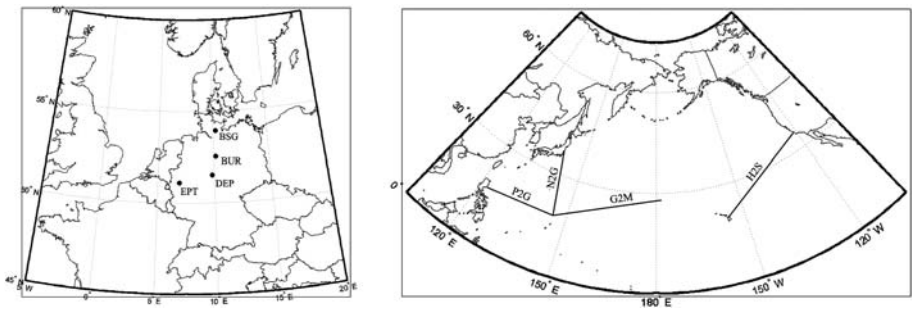

Fig. 32 Location of sites in northern Germany (left plot) and location of cables in the northern Pacific Ocean (right plot)

predicted voltages due to the M2 and O1 tides and the voltages derived by Fujii and Utada (2000) at four northern Pacific Ocean cables (see their location on Fig. 32, right hand plot). It is seen that the voltage predictions show no pronounced dependence on R. The largest changes are detected for M2 tide voltage at Philippine-Guam (P2G) cable, where the two orders of magnitude change of R leads to a doubling of the predicted signal. The weaker dependence of the voltage on R is not surprising, since the maximum effect due to the changes of R is observed in the electric signals at the sharp lateral contrast of conductivity, which is only a small part of the total voltages from the long submarine cables considered.

The predictions shown in Figs. 33 and 34 are, on the whole, in good agreement with observations. Agreement is especially encouraging for the cable data and suggests a lithosphere resistance in the range of $10^8\ \Omega\ m^2$–$10^9\ \Omega\ m^2$, consistent with the estimates obtained by independent methods, based on completely different data (e.g. Kuvshinov et al. 1999). However, as is seen from the Fig. 33, a visible discrepancy still exists for the northern Germany data (note that a well-known conductivity anomaly in northern Germany is only partly included in the conductivity model). This motivates further investigations, including, for example, improved Earth's conductivity or/and tidal models. Another possibility for further work is to attempt to estimate the lateral variability in R.

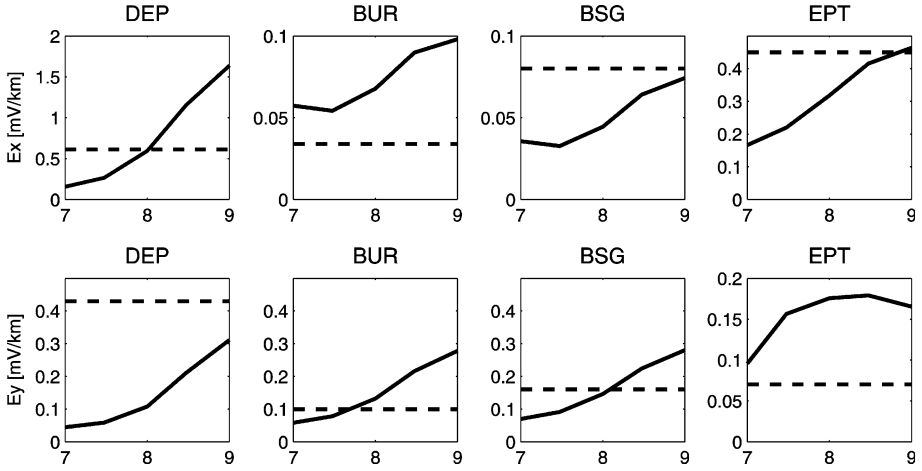

Fig. 33 Predicted amplitudes (solid curves as a functions of 10 log R) and observed amplitudes (dashed straight lines) of the M2 tide electric field in northern Germany. The upper and lower rows show the results for E_x and E_y components, respectively. After Kuvshinov et al. (2006b)

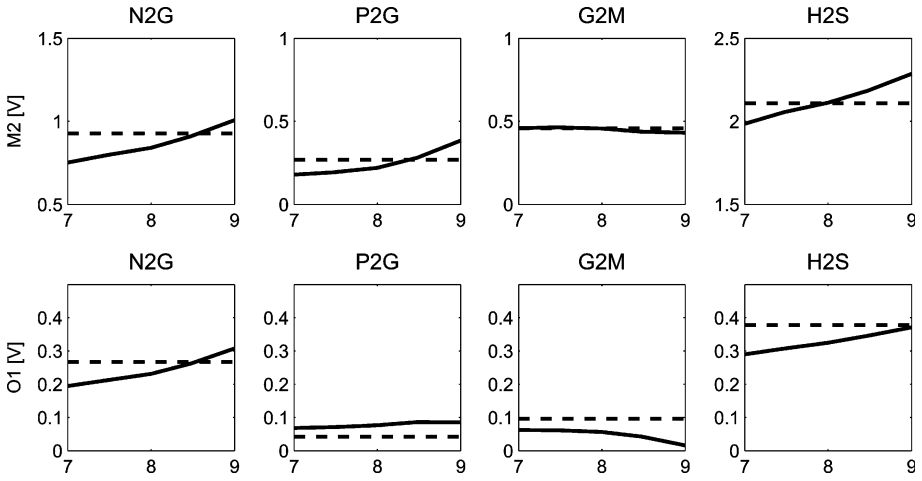

Fig. 34 Predicted amplitudes (solid curves as a functions of $\log_{10} R$) and observed amplitudes (dashed straight lines) of tidal voltages, V, from northern Pacific Ocean cables. The upper and lower rows show the results for the M2 and O1 tides, respectively. After Kuvshinov et al. (2006b)

8 Ocean Circulation

A further source of detectable magnetic signals above the Earth due to moving sea water is the global ocean circulation. Ocean circulation is driven by winds on the surface and density differences due to varying water temperature and salinity. Attempts to estimate ocean induced electric and/or magnetic fields due to realistic ocean circulation models have been made in a number of papers (e.g., Stephenson and Bryan 1992; Flosadottir et al. 1997; Tyler et al. 1997, 1998; Palshin et al. 1999; Vivier et al. 2004; Glazman and Golubev

2005; Manoj et al. 2006a). In particular, Vivier et al. (2004) attempt to correlate the variation in the simulated magnetic fields with the water transport across the Drake Passage between South America and Antarctica. They show that variability of the magnetic field is highly correlated with transport in the Antarctic Circumpolar Current (ACC).

There are, however, evident differences in this source compared with tides. First, one must consider now the steady flow rather than periodic tides and, secondly, the flow has a completely different velocity distribution. Figure 35 presents the depth integrated velocity compiled by Manoj et al. (2006a) from the ECCO (Estimating the Circulation and Climate of the Ocean) ocean circulation model. The main feature here is a prominent Antarctic Circumpolar Current. The ACC is the strongest ocean current in the world: it transports about 130 Sv (Sv $= 10^6$ m^3 s^{-1}) of water around Antarctica, which makes it the most significant exchanger of heat, salt, and momentum between the Atlantic, Indian and Pacific Oceans. Figure 36 shows the dominant ocean induced magnetic signal—vertical component—at sea level (left) and at the CHAMP altitude (right). The simulations are predominantly influenced by the ACC; the eastward flowing ACC results in two prominent anomalies to the East and West of the southern geomagnetic pole (located in the South Australian Ocean). Both at sea level and the CHAMP altitude, the predictions show a relatively significant contribution of the ocean circulation generated magnetic fields signals, with an amplitude range of ± 6 and ± 2 nT, respectively. The results of Manoj et al. (2006a) agree well with the previous results of Tyler et al. (1998) and Vivier et al. (2004). Because these three different studies involved two rather different numerical methods for calculation of the magnetic fields from the flow and three different parametrizations (say, different input ocean circulation models were used), there is now reasonable confidence about these results. Note, however, that Glazman and Golubev (2005) predict that the ocean circulation generated magnetic signals are much larger than the results of the above mentioned groups, reaching some tens of nT at sea level. Since no observations show such high magnetic signals due to ocean circulation, their prediction seems to be doubtful.

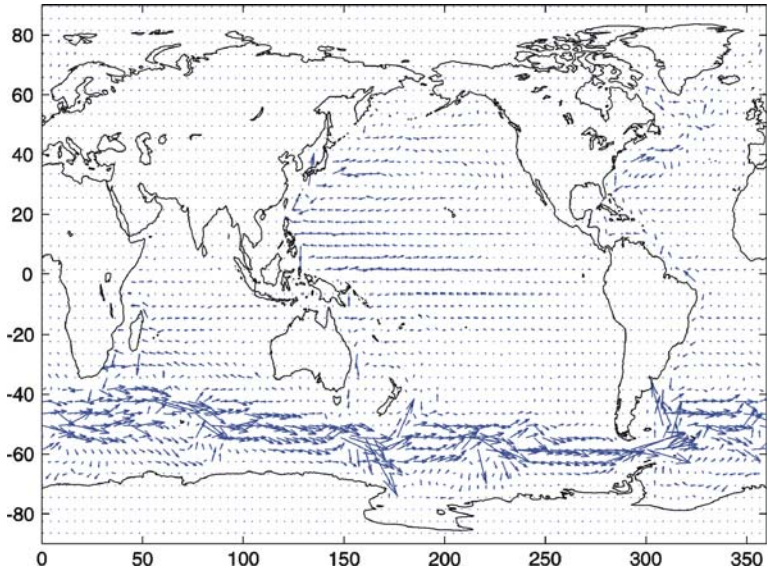

Fig. 35 Depth integrated velocity (in m^2/s) from the ECCO ocean circulation model. Maximum arrow length is 490 m^2/s. After Manoj et al. (2006a)

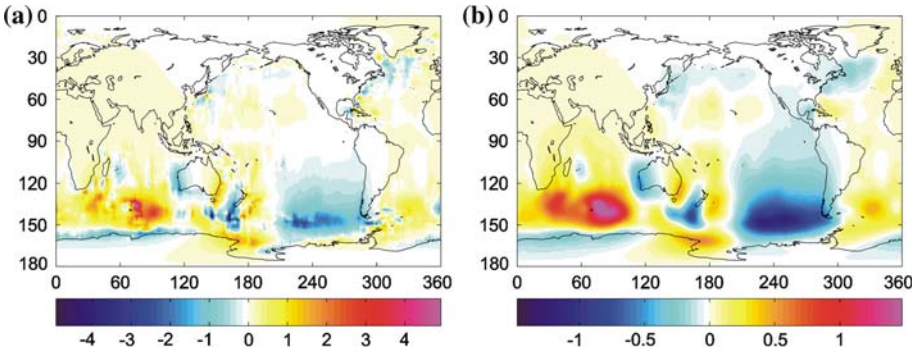

Fig. 36 Z (in nT) due to global ocean circulation at sea level (left panel) and at the CHAMP altitude (right panel). After Manoj et al. (2006a, b)

In contrast to tidal signals, the time-independent magnetic signals of the steady flow are extremely difficult to distinguish from the crustal magnetic field which in many regions has comparable or higher amplitudes at satellite altitudes. But, by analogy with the correction for tidal signals (cf. Maus et al. 2006), it would be worth investigating improving crustal field anomaly maps by subtracting predicted signals due to realistic ocean circulation models from the magnetic satellite observations.

While mean ocean magnetic signals may be difficult to remove from the crustal magnetic field, their temporal variation distinguishes them from the static crustal field. It may thus be possible to have an independent measure of ocean variability from satellite magnetometer records. Manoj et al. (2006a) estimate the total range of B_r variability from 1992–2002 month-to-month ECCO models at CHAMP altitudes (see Fig. 37). Relatively strong variability (about 0.5 nT) can be seen over the Southern Indian and Australian

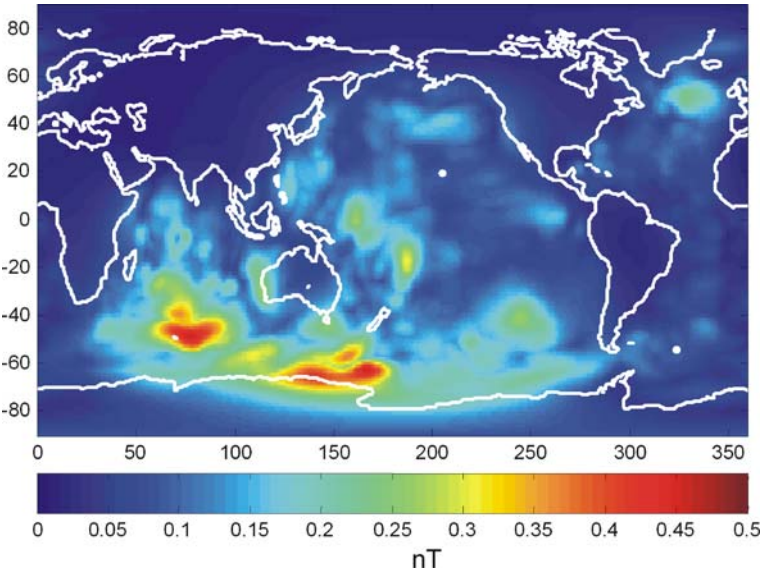

Fig. 37 The range of Z variability (in nT) due to global ocean circulation for the month-by-month 1992–2002 period at the CHAMP altitude. After Manoj et al. (2006a, b)

Oceans. This is most probably due to the combination of ACC flow variability and its proximity to the southern geomagnetic pole.

9 Tsunami

Following the devastating tsunami in the Indian Ocean on 26 December 2004, the detection and monitoring of tsunami-generated waves has received a high profile. Since motional induction in the ocean is sensitive to the movement of the entire water column (Flosadottir et al. 1997) this offers a possible way of monitoring of tsunami flow. Recently Tyler (2005) and Manoj et al. (2006b) estimated tsunami related magnetic signals. To compute these signals Manoj et al. (2006b) used a barotropic model (cf. Sindhu et al. 2007) of the Indian Ocean tsunami propagation. The model outputs (time series of North and East components of depth-integrated velocities) are generated for every $1^\circ \times 1^\circ$ cell and for every minute of a 6 h segment starting from the onset of the tsunami. The velocities at each cell were converted to the frequency domain and numerical simulations were performed independently for each frequency. Finally an inverse Fourier transform of the results was carried out to obtain the time series signals at each grid point. Figure 38 shows the range of the eastward (a) and southward (b) components of the depth-integrated velocities. Here, the range is defined as the difference between the maximum and minimum values of the velocities at each grid point during the entire period of simulation.

Figure 39 shows a map of the range of the predicted vertical magnetic signal at sea level due to the tsunami waves. The maximum amplitude of the signal is seen in the South Indian Ocean, because the major flow is directed towards the SW direction. As the main field B_r^m is a minimum near the geomagnetic dip-equator, the observed signals here have least strength. The maximum amplitude of the signal reaches 6 nT. The bathymetry control of the flow is also reflected in the predicted magnetic signals. The two stripes in the southern Indian Ocean are clearly due to the effect of the NS trending 90° E ridge in the Indian Ocean. The largest signal is seen in the South Indian Ocean, where it reaches 6 nT. Tyler (2005) proposed that the magnetic signal could possibly be detected and magnetic field measurements may be useful in future tsunami monitoring systems. Note that the range of the signals at a satellite altitude of 400 km (not shown here) are, however, less

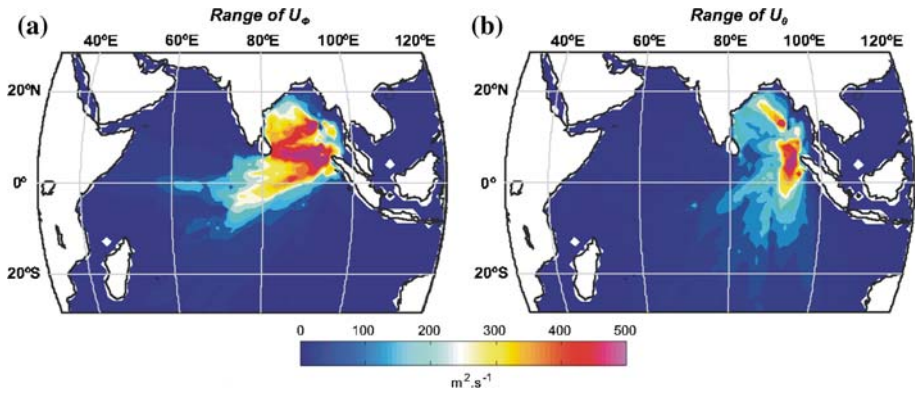

Fig. 38 Maps of the range of the eastward (**a**) and southward (**b**) components of the depth integrated velocities. This range is defined as the difference between the maximum and minimum values of the velocities at each grid point during the entire period of simulation. After Manoj et al. (2008)

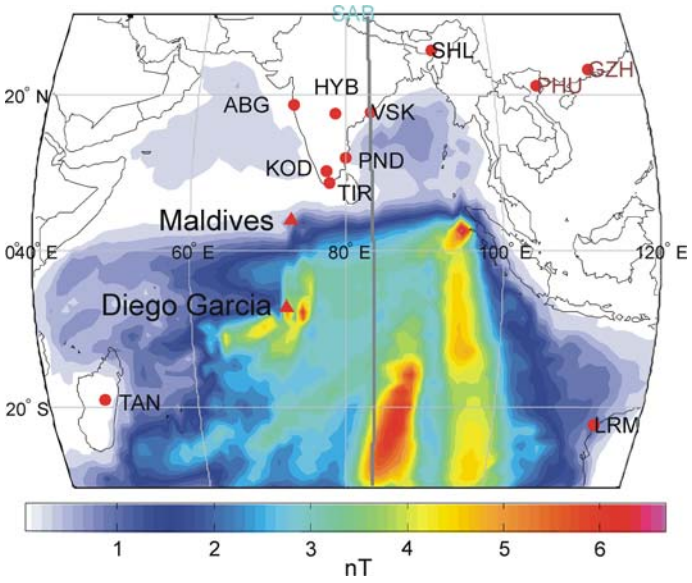

Fig. 39 Map of the range of the predicted magnetic vertical component at sea level due to the tsunami waves. The red circles and triangles are, respectively, existing and virtual magnetic observatories. After Manoj et al. (2006a, b)

than 0.2 nT. Compared to the magnetic signals generated by the ocean circulation and tidal flows, whose signal strengths at the satellite altitude are about ±1.5 nT, the tsunami-generated magnetic signals have much smaller amplitudes. One reason for this is the spatial scale of the tsunami flow: although it propagates for hundreds of kilometers, it is still of small scale when compared to the ocean circulation or tides.

Manoj et al. (2008) estimate the tsunami generated electric signals and investigate whether undersea cable voltage measurements can possibly detect the temporal variations of these electric fields. Figure 40 shows maps of the range of the horizontal electric field in

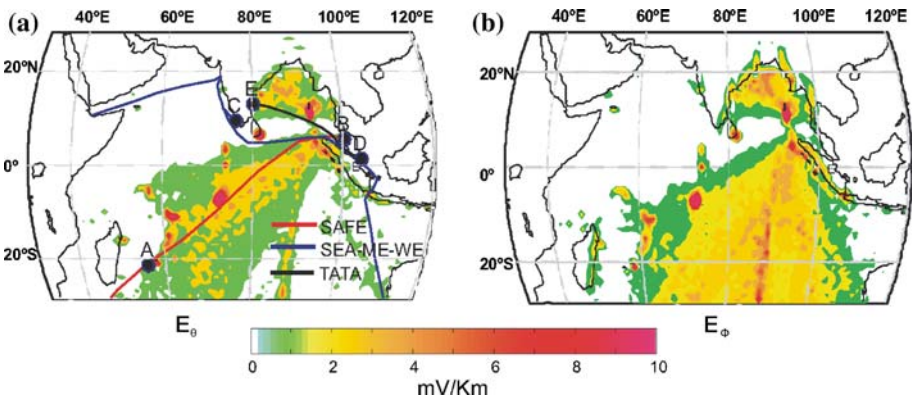

Fig. 40 Maps of the range of the southward (**a**) and eastward (**b**) components of the electric field. Coloured lines show the network of undersea communication cables in this region. The black circles are the endpoints of the cable. After Manoj et al. (2008)

the ocean induced by the Indian Ocean tsunami. The electric fields have strengths within the range ±10 mV/km, with the strongest signals being along the main flow region and near the coasts and islands. The topography control on the distribution of the electric field is evident. A band of low signal strength present parallel to 10° N latitude is due to the weak radial component of the main geomagnetic field. Manoj et al. (2008) also calculate the voltage difference along three in-service undersea cables in the Indian Ocean. They show that tsunami-induced electric voltages vary within ±500 mV across the existing submarine cables in the Indian Ocean, which is clearly a measurable signal (cf. Fujii and Utada 2000). The authors conclude that by using in-service or retired submarine cables to measure the electric potential across oceans, it may be possible to detect water movement related to a tsunami.

10 Conclusions

The numerical modeling studies reviewed here demonstrate that the 3-D induction effects and motionally-induced signals from the oceans contribute significantly to near-Earth magnetic and electric fields. These effects and signals can be predicted with the required accuracy and detail, both at the ground and at satellite altitudes, using modern 3-D numerical calculations. It is remarkable that the model predictions agree so well with observations. To conclude, a brief summary is given below of the most important results of 3-D numerical investigations of induction effects produced by the various sources considered in this review.

Magnetospheric storms

- During the main phase of the storm, the ocean effect is primarly manifested as a sharp field increase near the coasts, reaching some tens of nT both at sea level (80 nT maximum amplitude) and at the CHAMP altitude of 400 km (30 nT maximum amplitude). The effect is especially prominent near the Pacific coast of North America, and near the southern edges of Africa, Australia and South America (Kuvshinov and Olsen 2005a).
- The results for several major geomagnetic storms show much better agreement between the observed and the simulated time series of magnetic vertical component at coastal sites when the oceans are considered (Olsen and Kuvshinov 2004).
- Oceanic seawater is a major contributor to the anomalous behavior of *C*-responses at coastal observatories in the period range up to 20 days (Kuvshinov et al. 2002b).

Solar quiet (Sq) and equatorial electrojet (EEJ) variations

- Model studies demonstrate that the induction effect in *Z* due to the EEJ is negligible (comprising 1% of the external signal) everywhere *inland*, for all local times. Contrary to Sq, no coastal anomalous induction is generated by the EEJ. However, in the open ocean (e.g. in the eastern part of the Pacific Ocean) the EEJ induction effect is present, especially in the pre- and after-noon hours, when it can reach 50% of the external signal. Around local noon the induced signal in the ocean amounts to about 10% of the external signal. (The results due to Sq and EEJ sources summarized hereafter are taken from Kuvshinov et al. (2007).)
- At the CHAMP altitude, the EEJ induced signal above the oceans comprises only 2–5% of the external field at local noon. In particular, this means that one need not include induction effects when modeling the EEJ current strength from inland magnetic

measurements (including coastal regions) and/or satellite magnetic observations at local noon.

- Induction in the oceans strongly affects the Sq field in coastal regions. The intensity and the sign of the Sq coastal anomalies vary with local time and show different behaviors in different regions of the world. South India and Sri Lanka appear to be regions where prominent coastal anomalies are present during many local times.
- Kuvshinov et al. (2007) also show that the anomalous induction effect (defined as the difference between results obtained with and without induction in the oceans) of Sq is substantial at CHAMP and *Swarm* altitudes; around 12:30 LT it reaches 15 nT in oceanic regions and comprises more than 50% of the total Sq field. This means that the ocean effect in Sq variations should be considered in geomagnetic modeling, for example via a Comprehensive Modeling approach (Sabaka et al. 2004), involving both ground-based and satellite data.
- Induction in the oceans by Sq also generates small-scale anomalies of 8–10 nT intensity at ground level, even around local midnight in many coastal regions of the world (e.g., in Indonesia, South India, South West Africa). At the CHAMP altitude these anomalies have amplitudes of 2–3 nT. These results are relevant for lithospheric field determination where it is common practice to assume negligible non-polar ionospheric currents during night-time.
- A most striking finding is that the well-known anomalous behavior of the daily variations of Z at Indian electrojet sites, namely a large positive pre-noon peak, is entirely attributable to the ocean effect of Sq variations, with the EEJ playing no part. This result also implies that there is no need to assume a deep conductor in this region, which has been suggested by some authors to explain the observed anomaly in daily variations of Z.

Polar convection electrojet

- Model studies carried out as part of this review show that both at the surface and at the CHAMP altitude the 3-D induced signal from the polar convection electrojet is substantial and reaches one third of the external signal.
- The results for the 3-D Earth differ substantially from those for the 1-D Earth. The model with a perfect conductor (which is often used to account for induction in external field studies) gives a higher signal compared with the 3-D results, and reveals a very different spatial behavior (no time lag, with the amplitudes of the internal signal exactly following the external signal). The results for a realistic 1-D model are close in geometry to the 3-D results, but are much smaller in amplitude.
- The intensity of the induced signal varies with magnetic local time. It is a minimum in the afternoon and post-midnight (MLT) times and a maximum in the pre-noon and pre-midnight hours (see Sect. 6 of this review).
- The induction signal is substantially larger in the South Pole region than in the North due to a larger amount of deep ocean beneath the electrojet.

Ocean tides (magnetic fields)

- As was shown by Tyler et al. (2003), the magnetic fields generated by the lunar semidiurnal M2 ocean flow are clearly identified in magnetic satellite observations.
- In accordance with the geometry of the exciting current which is governed by the vertical component of the main magnetic field, the signals are negligible at the dip equator and increase towards the magnetic poles. Also the maxima of the magnetic field amplitudes follow those of the depth-integrated velocities, as expected. The

largest amplitudes of the M2 tidal magnetic field (about 5 nT at sea level) occur in the Indian Ocean, the western part of the South Pacific Ocean, in the North Pacific Ocean and in the North Atlantic Ocean. The magnitude at the CHAMP altitude is decreased (down to 2 nT) and is smoother compared to that at sea level (Kuvshinov and Olsen 2005b).

- The simulations of magnetic signals due to other tidal constituents (O1, S2, N2, K2, K1, P1, Q1) have revealed that their strength is much smaller than M2 (Kuvshinov and Olsen 2005b). But, as was demonstrated by Maus et al. (2006), by accumulating the predicted results from all tidal components it is possible to suppress tidal noise in the CHAMP observations.

Ocean tides (electric fields)

- Maximum tidal electric fields are detected on the coasts and have measurable amplitudes, reaching 10 mV/km and 100 mV/km for the O1 and M2 tides, respectively (The results for tidal electric signals summarized hereafter are taken from Kuvshinov et al. 2006b).
- Tidal electric fields are sensitive to variations in lithosphere resistance. On an average, a two order of magnitude change in resistance leads to a one order magnitude change in the coastal electric signal. This means that tidal electric fields can be used for sounding the high-resistive lithosphere.
- The predictions as a whole are in a good agreement with observed tidal electric fields measured at northern German sites and tidal voltages measured in northern Pacific Ocean cables. The agreement is especially encouraging for the cable data, and suggests lithosphere resistance in the range of 10^8 Ω m^2 and 10^9 Ω m^2.

Ocean circulation

- At sea level and the CHAMP altitude the predictions indicate that the ocean circulation generated magnetic fields signals have an amplitude range of ±6 and ±2 nT, respectively (Tyler et al. 1997; Vivier et al. 2004; Manoj et al. 2006a).
- The simulated magnetic fields are predominantly influenced by the Antarctic Circumpolar Current; the eastward flowing ACC results in two prominent anomalies to the East and West of the southern geomagnetic pole located in the South Australian Ocean (Vivier et al. 2004; Manoj et al. 2006a).
- In contrast to tidal signals, the time-independent magnetic signal of the steady flow is extremely difficult to distinguish from the crustal magnetic field. But, by analogy with the correction for tidal signals, it is probably reasonable to correct crustal field anomaly maps by subtracting predicted signals due to realistic ocean circulation models from the magnetic satellite observations.
- The variability of magnetic field at the CHAMP altitude due to variability of the ocean circulation is small and does not exceed 0.5 nT, with maximum values over the Southern Indian and Australian Oceans (Manoj et al. 2006a). It is unlikely that such variability can be detected by low-orbiting satellites, since 0.5 nT is very close to the accuracy of the satellite measurements.

Tsunami

- The magnetic signal due to the Sumatra tsunami might be observable in the South Indian Ocean, where it is expected to reach 6 nT at sea level (Tyler 2005; Manoj et al. 2006b). The range of the signals at the CHAMP altitude of 400 km was, however, less than 0.2 nT (Manoj et al. 2006b).

- Tsunami-generated electric fields have amplitudes in the range ±10 mV/km; strong signals along the main flow region and near the coasts and islands (Manoj et al. 2008).
- As demonstrated by Manoj et al. (2008), it may be possible to detect the water movement related to a tsunami using in-service or retired submarine cables to measure the electric potential across oceans.

The results described in this review, including conductance maps, 1-D cross-sections, 3-D predictions due to ocean tides and ocean circulation and movies visualizing the daily variations of EEJ and Sq, etc., can be downloaded from www.epm.geophys.ethz.ch/~kuvshinov.

Acknowledgements I wish to express my sincere thanks to the Managing Editor of the journal, Prof. Michael Rycroft, who offered me the opportunity to prepare and deliver this review. Most of the results presented in this review have been obtained in a close collaboration with Nils Olsen and Chandrasekharan Manoj. The author appreciates very much their contributions. I thank Chris Finlay who helped me to improve the English presentation of this review and made many valuable comments. I am grateful to Bob Parker and Cathy Constable for providing the multi-taper code. I wish to thank Richard Holme and an anonymous referee for helpful suggestions on how to improve the manuscript. This work has been supported in part by European Space Agency through contract No. 20944/07/NL/JA and by the Russian Foundation for Basic Research under grant No. 06-05-64329-a.

Appendices

Appendix 1: Governing Equations of the 3-D Volume Integral Equation Approach

The 3-D Earth model considered consists of a number of 3-D inhomogeneities of conductivity $\sigma_{3D}(r, \vartheta, \varphi)$, embedded in 1-D host section of conductivity $\sigma_b(r)$. Complex-valued conductivity σ(σ_{3D} and σ_b) can incorporate the effects of displacement currents or induced polarization. Note, also, that σ_{3D} may account for anisotropy of the electric conductivity and thus it is represented in general by a 3×3 matrix. For this problem statement, the EM fields in the frequency domain obey Maxwell's equations (1). Equations (1) are solved by a modern version of the volume integral equation approach. A brief review of the approach is given below.

First, some "reference" radially-symmetric (1-D) section of conductivity $\sigma_o(r)$ is introduced. The electric, $\mathbf{E}^o$, and magnetic, $\mathbf{H}^o$, fields in the reference medium obey Maxwell's equations

$$\nabla \times \mathbf{H}^o = \sigma_o \mathbf{E}^o + \mathbf{j}^{ext}, \quad \nabla \times \mathbf{E}^o = i\omega\mu_o \mathbf{H}^o, \tag{A.1.1}$$

and can be determined via fundamental solutions (dyadic Green's functions) of Eq. A.1.1, G_o^{ej} and G_o^{hj} as

$$\mathbf{E}^o = \int_{V^{ext}} G_o^{ej}(\mathbf{r}, \mathbf{r}') \mathbf{j}^{ext}(\mathbf{r}') dv', \quad \mathbf{H}^o = \int_{V^{ext}} G_o^{hj}(\mathbf{r}, \mathbf{r}') \mathbf{j}^{ext}(\mathbf{r}') dv'. \tag{A.1.2}$$

Here V^{ext} is the volume occupied by $\mathbf{j}^{ext}$, $\mathbf{r} = (r, \vartheta, \varphi), \mathbf{r}' = (r', \vartheta', \varphi')$. Explicit forms for dyadic Green's functions G_o^{ej} and G_o^{hj} are presented in Appendix 2. Introducing "scattered" fields, $\mathbf{E}^s = \mathbf{E} - \mathbf{E}^o$ and $\mathbf{H}^s = \mathbf{H} - \mathbf{H}^o$, and subtracting (A.1.1) from (1), Maxwell's equations for the scattered fields are obtained

$$\nabla \times \mathbf{H}^s = \sigma_o \mathbf{E}^s + \mathbf{j}^q, \quad \nabla \times \mathbf{E}^s = i\omega\mu_o \mathbf{H}^s, \tag{A.1.3}$$

where

$$\mathbf{j}^q = (\sigma - \sigma_o I)\mathbf{E}^s + \mathbf{j}^s, \quad \mathbf{j}^s = (\sigma - \sigma_o I)\mathbf{E}^o. \tag{A.1.4}$$

Here I is identity matrix. $\mathbf{E}^s$, in analogy with (A.1.2), can be written, as

$$\mathbf{E}^s = \int\limits_{V^{mod}} G_o^{ej}(\mathbf{r},\mathbf{r}')\mathbf{j}^q(\mathbf{r}')dv' = \mathbf{E}_o(\mathbf{r}) + \int\limits_{V^{mod}} G_o^{ej}(\mathbf{r}',\mathbf{r})(\sigma(\mathbf{r}') - \sigma_o(r')I)\mathbf{E}^s(\mathbf{r}')dv', \tag{A.1.5}$$

which gives the conventional scattering equation with respect to the unknown field $\mathbf{E}^s$, with a free term, $\mathbf{E}_o(\mathbf{r}) = \int_{V^{mod}} G_o^{ej}(\mathbf{r},\mathbf{r}')(\sigma(\mathbf{r}') - \sigma_o(\mathbf{r}')I)\mathbf{j}^s(\mathbf{r}')dv'$.Here V^{mod} is a region, where $\sigma - \sigma_o I$ differs from 0. After discretization, equation (A.1.5) can be solved by conjugate gradients (CG) iterations. However, for models with strong scatterers the resulting system of linear equations appears to be poorly conditioned. The remedy is to modify equation (A.1.5) to another integral equation (cf. Singer 1995; Pankratov et al. 1995, 1997)

$$\boldsymbol{\chi}(\mathbf{r}) - \int\limits_{V^{mod}} K(\mathbf{r},\mathbf{r}')R(\mathbf{r}')\boldsymbol{\chi}(\mathbf{r}')dv' = \boldsymbol{\chi}_o(\mathbf{r}), \tag{A.1.6}$$

where

$$R = (\sigma - \sigma_o I)(\sigma + \sigma_o^* I)^{-1}, \tag{A.1.7}$$

$$K(\mathbf{r},\mathbf{r}') = \delta(\mathbf{r} - \mathbf{r}')I + 2\sqrt{\mathrm{Re}\sigma_o(\mathrm{r})}G_o^{ej}(\mathbf{r},\mathbf{r}')\sqrt{\mathrm{Re}\sigma_o(r')}, \tag{A.1.8}$$

$$\boldsymbol{\chi}_o = \int\limits_{V^{mod}} K(\mathbf{r},\mathbf{r}')\sqrt{\mathrm{Re}\sigma_o}(\sigma + \sigma_o^* I)^{-1}\mathbf{j}^s(\mathbf{r}')dv', \tag{A.1.9}$$

where $\delta(\mathbf{r} - \mathbf{r}')$ is Dirac's delta function, σ_o^* and $\mathrm{Re}\sigma_o$ are the respective complex conjugate and real part of σ_o, and where

$$\boldsymbol{\chi} = \frac{1}{2\sqrt{\mathrm{Re}\sigma_o}}((\sigma + \sigma_o^* I)\mathbf{E}^s + \mathbf{j}^s). \tag{A.1.10}$$

Note that in order to derive (A.1.6) the term $(\sigma - \sigma_o)\mathbf{E}^o/2\mathrm{Re}\sigma_o$ is added to both sides of (A.1.5) and a change of variables is performed. The specific form of equation (A.1.6) is motivated by the energy inequality for the scattered EM field, which expresses a fundamental physical fact that the energy flow of the scattered field outside the domain with inhomogeneities is always non-negative (cf. Singer 1995; Pankratov et al. 1995). The advantage of this form of integral equation is that operator A

$$A\boldsymbol{\chi} = (I - KR)\boldsymbol{\chi} = \boldsymbol{\chi}_o, \tag{A.1.11}$$

is well conditioned irrespective of the conductivity contrast in the model. Indeed it can be shown (cf. Avdeev et al. 2000) that a condition number, $k(A) = \|A\| \cdot \left\|A^{-1}\right\|$, can be estimated as $k(A) \simeq \sqrt{M}$, where M is the maximum lateral contrast in the model, provided the reference medium is chosen in an "optimal" way (Singer 1995). Specifically, outside the depths occupied by inhomogeneities, the reference medium coincides with the conductivity of the host section, $\sigma_b(r)$, but at depths with a laterally inhomogeneous distribution of conductivity it has a form $\sigma_o(r) = \sqrt{\min\limits_{\vartheta,\varphi}\sigma(r,\vartheta,\varphi)\max\limits_{\vartheta,\varphi}\sigma(r,\vartheta,\varphi)}$. From the estimate for $k(A)$ it follows that even for media with large lateral contrasts of conductivity (say, on land-ocean boundaries), the operator A still remains well conditioned.

Numerical solutions based on this volume integral approach can be represented schematically as a sequence of the following steps:

(1) A discretized form of A cf. (A.1.11) is calculated on V^{mod} (cf. (A.1.7) and (A.1.8));
(2) $\mathbf{j}^{\mathrm{s}}$ and $\boldsymbol{\chi}_{\mathrm{o}}$ are calculated on V^{mod} (cf. (A.1.4) and (A.1.9));
(3) The scattering equation (A.1.6) is solved on V^{mod} by the CG iterations;
(4) $\mathbf{E}^{\mathrm{s}}$ is calculated on V^{mod} from (A.1.10), and then $\mathbf{j}^{q}$ is calculated from (A.1.4);
(5) $\mathbf{E}^{\mathrm{s}}$ and $\mathbf{H}^{\mathrm{s}}$ are calculated at $\mathbf{r} \in V^{obs}$ (region of interest) as

$$\mathbf{E}^{\mathrm{s}} = \int\limits_{V^{mod}} G_{\mathrm{o}}^{ej}(\mathbf{r},\mathbf{r}')\mathbf{j}^{q}(\mathbf{r}')dv', \quad \mathbf{H}^{\mathrm{s}} = \int\limits_{V^{mod}} G_{\mathrm{o}}^{hj}(\mathbf{r},\mathbf{r}')\mathbf{j}^{q}(\mathbf{r}')dv'; \tag{A.1.12}$$

(6) $\mathbf{E}^{\circ}$ and $\mathbf{H}^{\circ}$ are calculated at $\mathbf{r} \in V^{obs}$ from (A.1.2) and finally the total fields are calculated as $\mathbf{E} = \mathbf{E}^{\mathrm{s}} + \mathbf{E}^{\circ}$ and $\mathbf{H} = \mathbf{H}^{\mathrm{s}} + \mathbf{H}^{\circ}$;

The cornerstone of the integral equation solution is the derivation and calculation of dyadic Green's functions, $G_{\mathrm{o}}^{ej}(\mathbf{r},\mathbf{r}')$ and $G_{\mathrm{o}}^{hj}(\mathbf{r},\mathbf{r}')$which are discussed below.

Appendix 2: Explicit Forms of 3 × 3 Dyadic Green's Functions of Radially-Symmetric Section

In this Appendix the final expressions for the elements of 3 × 3 dyadic Green's functions of radially-symmetric section, $G_{\mathrm{o}}^{ej}(\mathbf{r},\mathbf{r}')$ and $G_{\mathrm{o}}^{hj}(\mathbf{r},\mathbf{r}')$ are presented. The details of the derivation can be found in Kuvshinov (2008). These functions express electric and magnetic fields induced in a radially-symmetric section of conductivity $\sigma_{\mathrm{o}}(\mathrm{r})$ by an impressed current $\mathbf{j}$

$$\mathbf{E}(r,\vartheta,\varphi) = \int\limits_{V} G_{\mathrm{o}}^{ej}(r,r',\vartheta,\vartheta',\varphi-\varphi')\mathbf{j}(r',\vartheta',\varphi')dv', \tag{A.2.1}$$

$$\mathbf{H}(r,\vartheta,\varphi) = \int\limits_{V} G_{\mathrm{o}}^{hj}(r,r',\vartheta,\vartheta',\varphi-\varphi')\mathbf{j}(r',\vartheta',\varphi')dv'. \tag{A.2.2}$$

Here V is a 3-D volume occupied by a current $\mathbf{j}$, $dv' = r'^2 \sin\vartheta' d\vartheta' d\varphi' dr'$, and $G^{ej(hj)}$ are

$$G_{\mathrm{o}}^{ej(hj)} = \mathbf{e}_{\vartheta} g_{\vartheta\vartheta'}^{ej(hj)} \mathbf{e}_{\vartheta'} + \mathbf{e}_{\vartheta} g_{\vartheta\varphi'}^{ej(hj)} \mathbf{e}_{\varphi'} + \cdots + \mathbf{e}_{r} g_{rr'}^{ej(hj)} \mathbf{e}_{r'}, \tag{A.2.3}$$

where $\mathbf{e}_{\vartheta}$, $\mathbf{e}_{\varphi}$ and $\mathbf{e}_{r}$, $\mathbf{e}_{\vartheta'}$, $\mathbf{e}_{\varphi'}$ and $\mathbf{e}_{r'}$ are the unit vectors of spherical system of coordinates at points (r,ϑ,φ) and (r',ϑ',φ') respectively. For example if Eqs. A.1.12 are considered then $\mathbf{E} \equiv \mathbf{E}^{\mathrm{s}}$, $\mathbf{H} \equiv \mathbf{H}^{\mathrm{s}}$, $\mathbf{j} \equiv \mathbf{j}^{q}$, $V \equiv V^{\mathrm{mod}}$. The expressions for elements $g_{\vartheta\vartheta'}^{ej(hj)}$, $g_{\vartheta\varphi'}^{ej(hj)}$ … are

$$g_{\vartheta\vartheta'}^{ej} = \frac{1}{\sin\vartheta}\frac{1}{\sin\vartheta'}\partial_{\varphi}\partial_{\varphi'}P\left[\frac{1}{r'r}\frac{G^{t}}{n(n+1)}\right] + \partial_{\vartheta}\partial_{\vartheta'}P\left[\frac{1}{r'r}\frac{G^{p}}{n(n+1)}\right], \tag{A.2.4}$$

$$g_{\vartheta\varphi'}^{ej} = -\frac{1}{\sin\vartheta}\partial_{\varphi}\partial_{\vartheta'}P\left[\frac{1}{r'r}\frac{G^{t}}{n(n+1)}\right] + \frac{1}{\sin\vartheta'}\partial_{\vartheta}\partial_{\varphi'}P\left[\frac{1}{r'r}\frac{G^{p}}{n(n+1)}\right], \tag{A.2.5}$$

$$g_{\vartheta r'}^{ej} = -\partial_{\vartheta}P\left[\frac{1}{r'^2 r}\frac{\beta^{p}G^{p}}{\sigma_{\mathrm{o}}(r')}\right], \tag{A.2.6}$$

$$g^{ej}_{\varphi\vartheta'} = -\frac{1}{\sin\vartheta'}\partial_\vartheta\partial_{\varphi'}P\left[\frac{1}{r'r}\frac{G^t}{n(n+1)}\right] + \frac{1}{\sin\vartheta}\partial_\varphi\partial_{\vartheta'}P\left[\frac{1}{r'r}\frac{G^p}{n(n+1)}\right], \tag{A.2.7}$$

$$g^{ej}_{\varphi\varphi'} = \partial_\vartheta\partial_{\vartheta'}P\left[\frac{1}{r'r}\frac{G^t}{n(n+1)}\right] + \frac{1}{\sin\vartheta}\frac{1}{\sin\vartheta'}\partial_\varphi\partial_{\varphi'}P\left[\frac{1}{r'r}\frac{G^p}{n(n+1)}\right], \tag{A.2.8}$$

$$g^{ej}_{\varphi r'} = -\frac{1}{\sin\vartheta}\partial_\varphi P\left[\frac{1}{r'^2r}\frac{\beta^p G^p}{\sigma_{\mathrm{o}}(r')}\right], \tag{A.2.9}$$

$$g^{ej}_{r\vartheta'} = \partial_{\vartheta'}P\left[\frac{1}{r'r^2}\frac{\alpha^p G^p}{\sigma_{\mathrm{o}}(r)}\right], \tag{A.2.10}$$

$$g^{ej}_{r\varphi'} = \frac{1}{\sin\vartheta'}\partial_{\varphi'}P\left[\frac{1}{r'r^2}\frac{\alpha^p G^p}{\sigma_{\mathrm{o}}(r)}\right], \tag{A.2.11}$$

$$g^{ej}_{rr'} = -\frac{\delta(r-r')\delta(\vartheta-\vartheta')\delta(\varphi-\varphi')}{\sin\vartheta' r'^2\sigma_{\mathrm{o}}(r)} + P\left[\frac{1}{r'^2r^2}\frac{n(n+1)\alpha^p\beta^p G^p}{\sigma_{\mathrm{o}}(r)\sigma_{\mathrm{o}}(r')}\right], \tag{A.2.12}$$

for electric field, and

$$g^{hj}_{\vartheta\vartheta'} = -\frac{1}{\sin\vartheta'}\partial_\vartheta\partial_{\varphi'}P\left[\frac{1}{r'r}\frac{\alpha^t G^t}{n(n+1)}\right] - \frac{1}{\sin\vartheta}\partial_\varphi\partial_{\vartheta'}P\left[\frac{1}{r'r}\frac{\alpha^p G^p}{n(n+1)}\right], \tag{A.2.13}$$

$$g^{hj}_{\vartheta\varphi'} = -\frac{1}{\sin\vartheta}\frac{1}{\sin\vartheta'}\partial_\varphi\partial_{\varphi'}P\left[\frac{1}{r'r}\frac{\alpha^t G^t}{n(n+1)}\right] + \partial_\vartheta\partial_{\vartheta'}P\left[\frac{1}{r'r}\frac{\alpha^p G^p}{n(n+1)}\right], \tag{A.2.14}$$

$$g^{hj}_{\vartheta r'} = \frac{1}{\sin\vartheta}\partial_\varphi P\left[\frac{1}{r'^2r}\frac{\alpha^p\beta^p G^p}{\sigma_{\mathrm{o}}(r')}\right], \tag{A.2.15}$$

$$g^{hj}_{\varphi\vartheta'} = \partial_\vartheta\partial_{\vartheta'}P\left[\frac{1}{r'r}\frac{\alpha^t G^t}{n(n+1)}\right] - \frac{1}{\sin\vartheta'}\partial_\vartheta\partial_{\varphi'}P\left[\frac{1}{r'r}\frac{\alpha^p G^p}{n(n+1)}\right], \tag{A.2.16}$$

$$g^{hj}_{\varphi\varphi'} = \frac{1}{\sin\vartheta}\partial_\varphi\partial_{\vartheta'}P\left[\frac{1}{r'r}\frac{\alpha^t G^t}{n(n+1)}\right] + \frac{1}{\sin\vartheta'}\partial_\vartheta\partial_{\varphi'}P\left[\frac{1}{r'r}\frac{\alpha^p G^p}{n(n+1)}\right], \tag{A.2.17}$$

$$g^{hj}_{\varphi r'} = -\partial_\vartheta P\left[\frac{1}{r'^2r}\frac{\alpha^p\beta^p G^p}{\sigma_{\mathrm{o}}(r')}\right], \tag{A.2.18}$$

$$g^{hj}_{r\vartheta'} = \frac{1}{\sin\vartheta'}\partial_{\varphi'}P\left[\frac{1}{r'r^2}\frac{G^t}{i\omega\mu_{\mathrm{o}}}\right], \tag{A.2.19}$$

$$g^{hj}_{r\varphi'} = -\partial_{\vartheta'}P\left[\frac{1}{r'r^2}\frac{G^t}{i\omega\mu_{\mathrm{o}}}\right], \tag{A.2.20}$$

$$g^{hj}_{rr'} = 0 \tag{A.2.21}$$

for magnetic field. Here $P[f]$ stands for the summation of the series

$$P[f](\cos\gamma, r, r') = \sum_{n=0}^{\infty}\frac{2n+1}{4\pi}f(n,r,r')P_n(\cos\gamma), \tag{A.2.22}$$

where $\cos\gamma = \cos\vartheta\cos\vartheta' + \sin\vartheta\sin\vartheta'\cos(\varphi-\varphi')$, and P_n are Legendre polynomials. Scalar Green's functions $G^{t(p)}(n,r,r')$ are given as continuous solutions of equation

$$\partial_r\left(\frac{1}{p^{t(p)}(r)}\partial_r G^{t(p)}(n,r,r')\right) = q^{t(p)}(r)G^{t(p)}(n,r,r') + \delta(r-r'), \tag{A.2.23}$$

with the boundary conditions $G^{t(p)}(n,r,r') \to 0$ when $r \to 0$ and $r \to \infty$. The coefficients $p^{t(p)}(r)$ and $q^{t(p)}(r)$ are determined either as

$$p^t(r) = -i\omega\mu_o, \quad q^t(r) = -\frac{\kappa^2}{i\omega\mu_o}, \tag{A.2.24}$$

for the toroidal mode, or

$$p^p(r) = \frac{\kappa^2}{\sigma_o(r)}, \quad q^p(r) = \sigma_o(r), \tag{A.2.25}$$

for the poloidal mode. Here $\kappa^2 = n(n+1)/r^2 - i\omega\mu_o\sigma_o(r)$. The final result for $G^{t(p)}(n,r,r')$ is given as

$$G^{t(p)}(n,r,r') = -\frac{1}{Y^{l,t(p)}(n,r') + Y^{u,t(p)}(n,r')}\mathrm{e}^{\int_{r'}^{r} p^{t(p)}(n,\xi)\alpha^{t(p)}(n,\xi,r')d\xi}, \tag{A.2.26}$$

where the function $\alpha^{t(p)}(n,\xi,r')$ is

$$\alpha^{t(p)}(n,\xi,r') = \begin{cases} -Y^{u,t(p)}(n,\xi), & \xi > r' \\ Y^{l,t(p)}(n,\xi), & \xi < r' \end{cases}. \tag{A.2.27}$$

Note that the functions $\beta^{t(p)}$ in Eqs. A.2.6, A.2.9, A.2.12, A.2.15 and A.2.18 are defined via $\alpha^{t(p)}$ as $\beta^{t(p)}(n,r,r') = \alpha^{t(p)}(n,r',r)$.

It is seen from Eqs. A.2.26–A.2.27 that calculation of $G^{t(p)}(n,r,r')$ for arbitrary r and r' requires calculation of admittances $Y^{l,t(p)}(r')$ and $Y^{u,t(p)}(r')$, and calculations of exponentials, which in its turn contain $Y^{l,t(p)}$ and $Y^{u,t(p)}$. In order to calculate these functions radially-symmetric sections are introduced that consist of N layers $\{r_{k+1} < r \le r_k\}_{k=1,2,\ldots,N}$, where within each layer the conductivity varies as $\sigma_o(r) = \sigma_k\left(\frac{r_k}{r}\right)^2$ (e.g. Fainberg et al. 1990). Then the recurrences for calculating $Y^{p,l}(r_k)$, $Y^{p,u}(r_k)$, $Y^{t,l}(r_k)$ and $Y^{t,u}(r_k)$ for arbitrary r_k are

$$Y_k^{l,p} \equiv Y^{l,p}(r_k) = g_k\frac{Y_{k+1}^{l,p}(b_k - 0.5\tau_k) - g_k\eta_k\tau_k}{g_k\eta_k(b_k + 0.5\tau_k) - b_k^+ b_k^-\tau_k Y_{k+1}^{l,p}}, \quad k = N-1,\ \ldots,2,\ 1,\ Y_N^{l,p} = \frac{\sigma_N r_N}{b_N^-}, \tag{A.2.28}$$

$$Y_{k+1}^{u,p} = g_k\eta_k\frac{Y_k^{u,p}(b_k + 0.5\tau_k) - g_k\tau_k}{g_k(b_k - 0.5\tau_k) - b_k^+ b_k^-\tau_k Y_k^{u,p}}, \quad k = 1,\ 2,\ldots,N-1, \quad Y_1^{u,p} = \frac{\sigma_1 r_1}{b_1^+}, \tag{A.2.29}$$

$$Y_k^{l,t} = \frac{1}{q_k}\frac{q_{k+1}Y_{k+1}^{l,t}(b_k - 0.5\tau_k) + b_k^+ b_k^-\tau_k}{(b_k + 0.5\tau_k) + q_{k+1}\tau_k Y_{k+1}^{l,t}}, \quad k = N-1,\ \ldots,2,1, \quad Y_N^{l,t} = -\frac{b_N^+}{q_N}, \tag{A.2.30}$$

$$Y_{k+1}^{u,t} = \frac{1}{q_{k+1}}\frac{q_k Y_k^{u,t}(b_k + 0.5\tau_k) + b_k^+ b_k^-\tau_k}{(b_k - 0.5\tau_k) + q_k\tau_k Y_k^{u,t}}, \quad k = 1,\ 2,\ldots,N-1, \quad Y_1^{u,t} = -\frac{b_1^-}{q_1}, \tag{A.2.31}$$

where $q_k = i\omega\mu_o r_k, b_k^- = b_k - \frac{1}{2}, \quad b_k^+ = b_k + \frac{1}{2}, \quad b_k = \{(n+\frac{1}{2})^2 - i\omega\mu_0\sigma_k r_k^2\}^{\frac{1}{2}}, \eta_k = \frac{r_k}{r_{k+1}}$, $\tau_k = \frac{1-\varsigma_k}{1+\varsigma_k}$, $\varsigma_k = \eta_k^{2b_k}$ and $g_k = \sigma_k r_k$. Finally $G^{t(p)}(n,r_i,r_j)$ for $r_i < r_j$ can be written as

$$G^t(n,r_i,r_j) = -\frac{1}{Y_j^{t,\,l} + Y_j^{t,\,u}} \prod_{k=j}^{i} F_k^t, \quad r_i \le r_j,\ F_k^t = \frac{1}{1+\zeta_k} \frac{2b_k \eta_k^{b_k^-}}{(b_k + 0.5\tau_k) + q_k \tau_k Y_{k+1}^{l,t}}, \tag{A.2.32}$$

$$G^p(n,r_i,r_j) = -\frac{1}{Y_j^{p,\,l} + Y_j^{p,\,u}} \prod_{k=j}^{i} F_k^p,\ r_i \le r_j,\ F_k^p = \frac{1}{1+\zeta_k} \frac{2g_k b_k \eta_k^{b_k^-}}{g_k \eta_k (b_k + 0.5\tau_k) - b_k^+ b_k^- \tau_k Y_{k+1}^{l,p}}. \tag{A.2.33}$$

Note that, due to the symmetry of scalar Green's functions, $G^{t(p)}(n,r,r') = G^{t(p)}(n,r',r)$, one can readily obtain the results for $r_i > r_j$. Finally, it is relevant to mention that C-responses, C_n, at the Earth's surface are connected to $Y_1^{l,t}$ as

$$C_n = -1/i\omega\mu_o Y_1^{l,t}, \tag{A.2.34}$$

whereas Q_n are connected with $Y_1^{l,t}$ as

$$Q_n = \frac{n}{n+1} \frac{i\omega\mu_o a\, Y_1^{l,t} + n + 1}{i\omega\mu_o a\, Y_1^{l,t} - n}. \tag{A.2.35}$$

References

Ashour AA (1965) Electromagnetic induction in finite thin sheets. Quart J Mech Appl Math 18:73–86

Avdeev DB, Kuvshinov AV, Pankratov OV, Newman GA (2000) 3D EM modeling using fast integral equation approach with Krylov subspaces accelerator. Extended abstracts book, vol 2, 62nd EAGE Conference & Technical Exhibition, Glasgow, Scotland, P-183

Avdeev DB, Kuvshinov AV, Pankratov OV, Newman GA (2002) Three-dimensional induction logging problems, part I: an integral equation solution and model comparisons. Geophysics 67:413–426

Baumjohann W, Treumann R (1996) Basic space plasma physics. Imperial College Press, London

Beamish D, Hewson-Browne RC, Kendall PC, Malin SRC, Quinney DA (1980) Induction in arbitrarily shaped oceans IV: Sq for a simple oceans. Geophys J R Astr Soc 60:435–443

Bullard EC, Parker RL (1970) Electromagnetic induction in the oceans. In: Maxwell AE (ed) The sea, vol 4, Chap 18. John Wiley, New York, pp 695–730

Chapman S (1951) The equatorial electrojet as detected from the abnormal electric current distribution above Huancayo and elsewhere. Arch Meteorol Geophys Bioklimatol Sec A4:368–390

Duffus HJ, Fowler NR (1974) On planetary voltages, ocean tides, and electric conductivity below the Pacific. Can J Earth Sci 11:873–892

Erofeeva S, Egbert G (2002) Efficient inverse modeling of barotropic ocean tides. J Ocean Atmos Technol 19:183–204

Everett ME, Schultz A (1996) Geomagnetic induction in a heterogeneous sphere: azimutally symmetric test computations and the response of an undulating 660-km discontinuity. J Geophys Res 101:2765–2783

Everett ME, Constable S, Constable CG (2003) Effects of near-surface conductance on global satellite induction responses. Geophys J Int 153:277–286

Fainberg EB, Kuvshinov AV, Singer BSh (1990) Electromagnetic induction in a spherical earth with non-uniform oceans and continents in electric contact with the underlying medium – I. Theory, method and example. Geophys J Int 102:273–281

Flosadottir AH, Larsen JC, Smith JT (1997) Motional induction in North Atlantic circulation models. J Geophys Res 102:10353–10372

Friis-Christensen E, Lühr H, Hulot G (2006) *Swarm*: a constellation to study the Earth's magnetic field. Earth, Planets Space 58:351–358

Fujii I, Utada H (2000) On geoelectric potential variations over a planetary scale. Mem Kakioka Magn Obs 29:1–71
Glazman R, Golubev Y (2005) Variability of the ocean-induced magnetic field predicted at sea surface and at satellite altitudes. J Geophys Res 110:C12011. doi:10.1029/2005JC002926
Grammatica N, Tarits P (2002) Contribution at satellite altitude of electromagnetically induced anomalies arising from a three-dimensional heterogeneously conducting Earth, using Sq as an inducing source field. Geophys J Int 151:913–923
Hamano Y (2002) A new time-domain approach for the electromagnetic induction problem in a three-dimensional heterogeneous earth. Geophys J Int 150:753–769
Harvey RR, Larsen J, Montaner R (1977) Electric field recording of tidal currents in the Strait of Magellan. J Geophys Res 82:3472–3476
Hewson-Brown RC, Kendall PC (1978) Some new ideas on induction in infinitely-conducting oceans of arbitrary shapes. Geophys J R Astr Soc 53:431–444
Hobbs BA (1981) A comparison of Sq analyses with model calculations. Geophys J R Astr Soc 66:435–447
Junge A (1988) The telluric field in northern Germany induced by tidal motion in North Sea. Geophys J Int 95:523–533
Koyama T, Shimizu H, Utada H (2002) Possible effects of lateral heterogeneity in the D″ layer on electromagnetic variations of core origin. Phys Earth Planet Int 129:99–116
Kuvshinov A (2007) Global 3-D EM induction in the solid Earth and the oceans. In: Spichak V (ed) Electromagnetic sounding of the Earth's interior, vol 1. Elsevier, Holland, pp 4–24
Kuvshinov A (2008) 3-D integral equation analysis of the global Schumann resonance. J Atmos Phys (in preparation)
Kuvshinov A, Olsen N (2005a) Modelling the ocean effect of geomagnetic storms at ground and satellite altitude. In: Reigber Ch, Lühr H, Schwintzer P, Wickert J (eds) Earth observation with CHAMP. Results from three years in orbit. Springer-Verlag, Berlin, pp 353–358
Kuvshinov A, Olsen N (2005b) 3-D modelling of the magnetic fields due to ocean tidal flow. In: Reigber Ch, Lühr H, Schwintzer P, Wickert J (eds) Earth observation with CHAMP. Results from three years in orbit. Springer-Verlag, Berlin, pp 359–366
Kuvshinov A, Olsen N (2006) A global model of mantle conductivity derived from 5 years of CHAMP, Ørsted and SAC-C magnetic data. Geophys Res Lett 33:L18301. doi:10.1029/2006GL027083
Kuvshinov AV, Pankratov OV, Singer BSh (1990) The effect of the oceans and sedimentary cover on global magnetovariational field distribution. Pure Appl Geophys 134:533–540
Kuvshinov AV, Avdeev DB, Pankratov OV (1999) Global induction by Sq and Dst sources in the presence of oceans: bimodal solutions for non-uniform spherical surface shells above radially symmetric Earth models in comparison to observations. Geophys J Int 137:630–650
Kuvshinov AV, Avdeev DB, Pankratov OV, Golyshev SA, Olsen N (2002a) Modelling electromagnetic fields in 3-D spherical earth using fast integral equation approach. In: Zhdanov MS, Wannamaker P (eds) Three-dimensional electromagnetics. Elsevier, Holland, pp 43–54
Kuvshinov AV, Olsen N, Avdeev DB, Pankratov OV (2002b) Electromagnetic induction in the oceans and the anomalous behavior of coastal C-responses for periods up to 20 days. Geophys Res Lett 29(12). doi:10.1029/2001GL014409
Kuvshinov AV, Utada H, Avdeev DB, Koyama T (2005) 3-D modelling and analysis of Dst *C*-responses in the North Pacific Ocean region, revisited. Geophys J Int 160:505–526
Kuvshinov A, Sabaka T, Olsen N (2006a) 3-D electromagnetic induction studies using the Swarm constellation: mapping conductivity anomalies in the Earth's mantle. Earth Planets Space 58:417–427
Kuvshinov A, Junge A, Utada H (2006b) 3-D modelling the electric field due to ocean tidal flow and comparison with observations. Geophys Res Lett. doi: 10.1029/2005GL025043
Kuvshinov A, Manoj C, Olsen N, Sabaka T (2007) On induction effects of geomagnetic daily variations from equatorial electrojet and solar quiet sources at low and middle latitudes. J Geophys Res 112:B10102. doi:10.1029/2007JB004955
Langel RA, Estes RH (1985) Large-scale near-Earth magnetic fields from external sources and the corresponding induced internal field. J Geophys Res 90:2487–2494
Lanzerotti LJ, Sayres CH, Medford LV, Kraus JS, Maclennan CJ (1992) Earth potential over 4000 km between Hawaii and California. Geophys Res Lett 19:1177–1180
Laske G, Masters G (1997) A global digital map of sediment thickness. EOS Trans. AGU 78 F483
Maus S, Kuvshinov A (2004) Ocean tidal signals in observatory and satellite magnetic measurements. Geophys Res Lett 31. doi: 10.1029/2004GL000634
Maus SM, Rother M, Hemant K, Stolle C, Lühr H, Kuvshinov A, Olsen N (2006) Earth's lithospheric magnetic field determined to spherical harmonic degree 90 from CHAMP satellite measurements. Geophys J Int 165:319–330

Manoj C, Kuvshinov AV, Maus S, Lühr H (2006a) Ocean circulation generated magnetic signals. Earth Planets Space 58:429–437
Manoj C, Neetu S, Kuvshinov AV, Harinarayana T (2006b) Magnetic fields, generated by the Indian ocean Tsunami. In: Proceedings of the first swarm international science meeting, Nant, France
Manoj C, Kuvshinov AV, Neetu S, Harinarayana T (2008) Can undersea voltage measurements detect tsunamis? Earth Planets Space (submitted)
Martinec Z (1999) Spectral-finite element approach to three-dimensional electromagnetic induction in a spherical Earth. Geophys J Int 136:229–250
Neubert T, Mandea M, Hulot G, von Frese R, Primdahl F, Jørgensen JL, Friis-Christensen E, Stauning P, Olsen N, Risbo T (2001) Ørsted satellite captures high-precision geomagnetic field data: EOS 82, No. 7, pp 81, 87, 88
Olsen N (1999) Induction studies with satellite data. Surv Geophys 20:309–340
Olsen N (2002) A model of the geomagnetic field and its secular variation for epoch 2000 estimated from Orsted data. Geophys J Int 149:454–462
Olsen N, Kuvshinov A (2004) Modelling the ocean effect of geomagnetic storms. Earth Planets Space 56:525–530
Onwumechili CA (1997) The equatorial electrojet. Gordon & Breach, Chap 2
Palshin N, Vanyan L, Yegorov I, Lebedev K (1999) Electric field induced by the global ocean circulation. Phys Solid Earth 35:1028–1035
Pankratov OV, Avdeev DB, Kuvshinov AV (1995) Electromagnetic field scattering in a heterogeneous earth: a solution to the forward problem. Phys Solid Earth 31:201–209
Pankratov OV, Kuvshinov AV, Avdeev DB (1997) High-performance three-dimensional electromagnetic modeling using modified Neumann series. Anisotropic case. J Geomagn Geoelectr 49:1541–1548
Plotkin VV (2004) Electromagnetic field in a nonuniform sphere (3D case), Russian. Geol Geophys 45(9):1107–1120
Pulkkinen A, Engels M (2005) The role of 3D geomagnetic induction in the determination of the ionospheric currents from ground-based data. Ann Geophysicae 23:909–917
Pulkkinen A, Amm O, Viljanen A and the Bear Working group (2003) Ionospheric equivalent current distributions determined with the method of spherical elementary current systems. J Geophys Res 108(A2):1053
Rastogi RG (2004) Electromagnetic induction by the equatorial electrojet. Geophys J Int 158:16–31
Reigber C, Lühr H, Schwintzer P (2002) CHAMP mission status. Adv Space Res 30:129–134
Riedel K, Sidorenko A (1995) Minimum bias multiple taper spectral estimation. IEEE Trans Signal Process 43:188–195
Rooney WJ (1938) Lunar diurnal variation in Earth currents at Huancayo and Tuscon. J Geophys Res 43:107–118
Rostoker G, Friedrich E, Dobbs M (1997) Physics of magnetic storms. In: Tsurutani BT, Gonzales WD, Kamide Y, Arballo JK (eds) 98 Geophysical monograph series, AGU, Washington DC, pp 149–160
Sabaka T, Olsen N, Purucker M (2004) Extending comprehensive models of the Earth's magnetic field with Orsted and CHAMP data. Geophys J Int 159:521–547
Sindhu BI, Suresh A, Unnikrishnan N, Bhatkar S, Neetu GS (2007) Michael, improved bathymetric datasets for the shallow water regions in the Indian Ocean. J Earth Syst Sci 116:261–274
Singer BSh (1995) Method for solution of Maxwell's equations in non-uniform media. Geophys J Int 120:590–598
Schmucker U (1985a) Electrical properties of the Earth's interior. In: Landolt-Bornstein, New Series, 5/2b. Springer-Verlag, Berlin, pp 370–395
Schmucker U (1985b) Magnetic and electric fields due to electromagnetic induction by external sources. In: Landolt-Bornstein, New Series, 5/2b. Springer-Verlag, Berlin, pp 100–125
Schmucker U (1999) A spherical harmonic analysis of solar daily variations in the years 1964–1965: response estimates and source fields for global induction – I. Methods. Geophys J Int 136:439–454
Stephenson D, Bryan K (1992) Large-scale electric and magnetic fields generated by the oceans. J Geophys Res 97:15467–15480
Takeda M (1991) Electric currents in the ocean induced by the geomagnetic Sq field and their effect on the estimation of mantle conductivity. Geophys J Int 104:381–385
Takeda M (1993) Electric currents in the ocean induced by model Dst field and their effects on the estimation of mantle conductivity. Geophys J Int 114:289–292
Tarits P (1994) Electromagnetic studies of global geodynamic processes. Surv Geophys 15:209–238
Tarits P, Grammatica N (2000) Electromagnetic induction effects by the solar quiet magnetic field at satellite altitude. Geophys Res Lett 27:4009–4012

Tyler RH (2005) A simple formula for estimating the magnetic fields generated by tsunami flow. Geophys Res Lett 32:L09608. doi:10.1029/2005GL022429
Tyler R, Mysak LA, Oberhuber J (1997) Electromagnetic fields generated by a 3-D global ocean circulation. J Geophys Res 102:5531–5551
Tyler R, Sanford TB, Oberhuber J (1998) Magnetic fields generated by ocean flow. AGU Fall Conference
Tyler R, Maus S, Lühr H (2003) Satellite observations of magnetic fields due to ocean tidal flow. Science 299:239–240
Utada H, Koyama T, Shimizu H, Chave A (2003) A semi-global reference model for electrical conductivity in the mid-mantle beneath the north Pacific region. Geophys Res Lett 30(4). doi: 10.1029/2002GL016092
Uyeshima M, Schultz A (2000) Geoelectromagnetic induction in a heterogeneous sphere: a new 3-D forward solver using a staggered-grid integral formulation. Geophys J Int 140:636–650
Vanyan LL, Palshin NA, Repin IA (1995) Deep magnetottelluric sounding with the use of the Australia-New Zealand cable 2. Interpretation. Phys Solid Earth 31:417–421
Velimsky J, Everett ME (2005) Electromagnetic induction by Sq ionospheric currents in a heterogeneous Earth: modelling using ground-based and satellite measurements: In: Reigber Ch, Lühr H, Schwintzer P, Wickert J (eds) Earth observation with CHAMP. Results from three years in orbit. Springer-Verlag, pp 341–347
Velimsky J, Martinec Z (2005) Time-domain, spherical harmonic-finite element approach to transient three-dimensional geomagnetic induction in a spherical heterogeneous Earth. Geophys J Int 161:81–101
Velimsky J, Everett ME, Martinec Z (2003) The transient Dst electromagnetic induction signal at satellite altitudes for a realistic 3-D electrical conductivity in the crust and mantle. Geophys Res Lett doi: 10.1029/2002GL016,671
Vivier F, Maier-Reimer E, Tyler RH (2004) Simulations of magnetic fields generated by the Antarctic Circumpolar Current at satellite altitude: can geomagnetic measurements be used to monitor the flow? Geophys Res Lett 31. doi:10.1029/2004GL019804
Wang H, Lühr H, Ma SY (2005) Solar zenith angle and merging electric field control of field-aligned currents: a statistical study of the southern hemisphere. J Geophys Res 110 A3, A03306 doi: 10.1029/2004JA010530
Weidelt P (1972) The inverse problem of geomagnetic induction. Z Geophys 38:257–289
Weiss CJ, Everett ME (1998) Geomagnetic induction in a heterogeneous sphere: fully three-dimensional test computations and the response of a realistic distribution of oceans and continents. Geophys J Int 135:650–662
Yoshimura R, Oshiman N (2002) Edge-based finite element approach to the simulation of geoelectromagnetic induction in a 3-D sphere. Geophys Res Lett 29(2). doi: 10.1029/2001GL014121